Title

Neuronal and astrocytic contributions to Huntington's disease dissected with zinc finger protein transcriptional repressors

Journal

Cell Reports, 42(1)

ISSN

2639-1856

Authors

Gangwani, Mohitkumar R
Soto, Joselyn S
Jami-Alahmadi, Yasaman
et al.

Publication Date

2023

DOI

10.1016/j.celrep.2022.111953

Peer reviewed

HHS Public Access

Author manuscript

Cell Rep. Author manuscript; available in PMC 2023 February 04.

Published in final edited form as:

Cell Rep. 2023 January 31; 42(1): 111953. doi:10.1016/j.celrep.2022.111953.

Neuronal and astrocytic contributions to Huntington's disease dissected with zinc finger protein transcriptional repressors

Mohitkumar R. Gangwani[1], **Joselyn S. Soto**[1], **Yasaman Jami-Alahmadi**[3], **Srushti Tiwari**[1], **Riki Kawaguchi**[4], **James A. Wohlschlegel**[3], **Baljit S. Khakh**[1,2,*]

[1]Department of Physiology, University of California Los Angeles. Los Angeles, CA 90095-1751, USA

[2]Department of Neurobiology, University of California Los Angeles. Los Angeles, CA 90095-1751, USA

[3]Department of Biological Chemistry, University of California Los Angeles. Los Angeles, CA 90095-1751, USA

[4]Center for Neurobehavioral Genetics, Semel Institute for Neuroscience and Human Behavior, University of California Los Angeles. Los Angeles, CA 90095-1751, USA

Summary

Huntington's disease (HD) is caused by expanded CAG repeats in the Huntingtin gene (*HTT*) resulting in expression of mutant HTT proteins (mHTT) with extended polyglutamine tracts, including in striatal neurons and astrocytes. It is unknown if pathophysiology *in vivo* can be attenuated by lowering mHTT in either cell type throughout the brain, and the relative contributions of neurons and astrocytes to HD remain undefined. We use zinc finger protein (ZFP) transcriptional repressors to cell-selectively lower mHTT *in vivo*. Astrocytes display loss of essential functions such as cholesterol metabolism that are partly driven by greater neuronal dysfunctions, which encompass neuromodulation, synaptic, and intracellular signaling pathways. Using transcriptomics, proteomics, electrophysiology, and behavior we dissect neuronal and astrocytic contributions to HD pathophysiology. Remarkably, brain wide delivery of neuronal ZFPs results in strong mHTT lowering, rescue of HD-associated behavioral and molecular phenotypes, and significant extension of lifespan, findings that support translational development.

Corresponding author: bkhakh@mednet.ucla.edu.

*Lead contact

Author contributions

MRG performed experiments and analyzed the data following direction from BSK and RK. JSS performed proteomic experiments/analyses and helped with RNA-seq. YJ-A performed mass spectrometry and provided proteomic analyses. ST helped with behavioral data analyses. RK performed RNA-seq data analyses and batch corrections. JAW provided guidance and supervision for the mass spectrometry runs and for the proteomic data. BSK performed some of the electrophysiology, conceived the study, planned and directed the experiments, and planned the figures with help from MRG and JSS. BSK wrote the paper; MRG and JSS helped. All authors contributed.

Declaration of interests

The authors declare no competing interests. Baljit S. Khakh is on the editorial advisory board of Neuron.

Introduction

Huntington's disease (HD) is a severe and terminal neurodegenerative disease that encompasses a triad of motor, cognitive, and psychiatric phenotypes [1]. The disease is caused by a single molecular defect: a CAG repeat expansion in exon 1 of the *HTT* gene. HD is inherited in an autosomal dominant manner [2], is 100% penetrant when the CAG repeat sequence exceeds 40, and the age of clinical onset is inversely correlated to the number of CAG repeats on the disease allele [1]. The CAG expansion within Exon 1 gives rise to a polyglutamine-tract expanded mutant HTT protein (mHTT) which is highly aggregation-prone, a pathological feature of the disease. The presence of mHTT initiates a cascade of cellular and molecular pathologies leading to cellular dysfunction, and ultimately to behavioral and phenotypic manifestations of the disease [3].

Although mHTT is expressed throughout the body, HD mainly affects the CNS with the striatum undergoing marked atrophy and dysfunction [4]. Much research over the last few decades has focused on understanding the molecular, cellular, and circuit underpinnings of HD pathophysiology. Evaluation of controls, post mortem human HD tissue and HD mouse models has shown that all major brain cell types express the Huntingtin gene and mHTT [5–8]. Both neurons and astrocytes develop mHTT protein aggregates [5,8–10], and display multiple molecular, cellular, and physiological disturbances [11–13]. Astrocytes and neurons are predominant cell types of the brain, but how dysfunction in each of these cell types contributes to HD pathophysiology has not been directly explored *in vivo*. Understanding the contributions of astrocytes and neurons to HD pathophysiology is necessary to elucidate causal disease-driving cellular mechanisms and to identify therapeutic opportunities. Further, and specifically for genetic strategies employing mHTT lowering, it is unknown whether regionally restricted or brain wide mHTT lowering will be required for meaningful clinical benefit, and whether it will be necessary to target either or both neurons and astrocytes.

We utilized genetically encoded zinc finger proteins (ZFP) carrying KRAB transcriptional repressor domains selective for the mutant *HTT* allele [14]. We assessed the consequences of lowering mHTT in astrocytes or neurons in turn for HD pathophysiology at molecular, cellular, and behavioral levels *in vivo*. We found that the major disease drivers were neurons, with astrocytes displaying lesser but significant loss of essential functions such as cholesterol metabolism that were partly downstream of neuronal dysfunction. Neuronal ZFPs resulted in strong neuron-specific mHTT lowering and rescue of molecular, physiological, and behavioral HD phenotypes, including lifespan extension when expressed throughout the CNS.

Results

Strategy

To determine how mHTT within astrocytes and neurons contributes to HD pathophysiology, we lowered mHTT within each cell type in the striatum in turn using a CAG-directed ZFP (ZFP-D also known as ZFP30645) that represses expression from the mHTT allele [14,15]. We reasoned that if mHTT in both astrocytes and neurons is causal to HD, then lowering

mHTT load in each cell type should reduce that cell type's contribution to pathophysiology, which we assessed at multiple levels. Since neurons and astrocytes may contribute to HD via cell-autonomous and non-cell autonomous mechanisms, we also determined how lowering mHTT load in either astrocytes or neurons impacted HD-associated molecular signatures in neurons or astrocytes, respectively (Figure 1A). We started by using a transgenic Exon 1 mHTT model (R6/2) that recalls juvenile onset HD [16,17], because multiple endpoints can be assessed, including robust behavioral phenotypes and survival analysis. All comparisons were made between R6/2 and non-carrier (NCAR) mice to assess HD-associated differentially expressed genes (DEGs). RiboTag approaches to isolate actively translated mRNAs were used with AAVs employing *GfaABC$_1$D* or *hSyn* promoters that target striatal astrocytes and neurons, respectively (Figure S1A–G). We also repeated key molecular experiments with neuronal ZFPs in the full-length mHTT knock-in zQ175 heterozygous HD mouse model. Genetically, this model has excellent construct validity in relation to human disease [7,18–23]. However, the heterozygous has relatively weak behavioral phenotypes, making it less suited to powered behavioral analysis [24–27].

The ZFP used in this study was chosen from those available because it had the least off-target CAG-repeat containing genes [14]. We assessed known off-target genes in our evaluations, but to control for their potential implications, all studies included the active ZFP in non-carrier (NCAR) or wild type (WT) mice, which assessed the impact of the repression of any off target genes on the measured biological endpoints. Additionally, a DNA-binding deleted ZFP (Delta), which cannot bind to the CAG repeat in the *HTT* gene, was used as a viral control (Figures 1C,F, 2A).

Striatal ZFPs lower mHTT in astrocytes and neurons *in vivo*

The aggregated form of mHTT is reliably detected using immunohistochemistry (IHC), whereas soluble mHTT cannot be distinguished from endogenous murine HTT by this method. IHC shows EM48-positive mHTT aggregates in the striatum of R6/2 mice at 3 months of age, but not in the NCAR controls [10,15,16]. Reproducing these data, using NeuN and S100β as markers for neurons and astrocytes, respectively, we found that ~98% of neurons and ~38% of astrocytes contained somatic mHTT aggregates (Figure 1B), which recalls past work [5,8,10]. Using the *GfaABC$_1$D* promoter, we used AAVs to express mHTT lowering HA-tagged ZFPs (A-ZFP) and non-DNA binding control ZFP constructs (A-Delta) in astrocytes along with tdTomato using a P2A sequence (Figure 1C). A-ZFP and A-Delta were expressed in ~80% of striatal astrocytes, but in negligible neurons (Figure S2A–C). tdTomato was also expressed in 80% of astrocytes and was not found in neurons (Figure S2A–C). Within astrocytes, mHTT aggregates were reduced significantly by ~70% by A-ZFP (Figure 1E). qPCR showed ~50% reduction of mHTT mRNA within astrocytes, with no effect on endogenous Htt mRNA levels (Figure 1D).

Similarly, using *hSyn* to target neurons, we generated AAVs to express mHTT lowering HA-tagged ZFPs (N-ZFP) and non-binding control ZFP constructs (N-Delta) along with tdTomato as a separate protein (Figure 1F). N-Delta and N-ZFP were expressed in ~98% of neurons, but negligibly in astrocytes (Figure S2D–F). Furthermore, tdTomato was expressed in ~82% of neurons and was not found in astrocytes (Figure S2D–F). Within neurons,

mHTT aggregates were found in ~98% of Darpp32 positive MSNs in the N-Delta group, but this was reduced by ~95% in the N-ZFP group (Figure 1H). qPCR evaluations showed ~84% reduction of mHTT mRNA within neurons, with no effect on endogenous wild type Htt mRNA levels (Figure 1G). The degree of mHTT lowering in neurons and astrocytes was similar when assessed with IHC whether ZFP and Delta-ZFP expression was assessed by virtue of the HA tag or by expression of the tdTomato (Figure 1E, H; Figure S3). Thus, astrocyte- and neuron-targeted ZFPs lowered mHTT levels in each cell type.

Cell autonomous and non-cell autonomous effects of striatal mHTT lowering

We used RNA sequencing (RNA-seq) to assess the effects of mHTT lowering in neurons or astrocytes[15]. The “disease group” compared gene expression differences between NCAR and R6/2 mice using RiboTag[28] for neurons or astrocytes following A-Delta and N-Delta microinjections (Figure 2A). Conversely, the “treatment group” compared gene expression differences between NCAR and R6/2 mice for neurons and astrocytes following A-ZFP and N-ZFP microinjections (Figure 2A), as previously reported for astrocytes[15]. In all cases, mice were injected with AAVs presymptomatically at four weeks of age and assessments were performed seven weeks later when the R6/2 mice were profoundly symptomatic (Figure 2B). We compared A-ZFP and N-ZFP to the combined Delta group. Astrocyte-specific RNA-seq data were enriched with 200 striatal astrocyte enriched genes [29], whereas neuronal RNA-seq data were enriched with 200 MSN genes (Figure S4A,B). Multidimensional scaling (MDS) across all groups separated astrocytic, neuronal, and bulk RNA-seq data (Figure 2C). The N-ZFP data were clustered closer to the Delta NCAR than the Delta R6/2 group, hinting N-ZFPs may have restored gene expression towards control.

The effect of A-ZFP and N-ZFP on HD-associated genes relative to Delta for both astrocytes and neurons was confirmed by differentially expressed gene (DEG) analyses (false discovery rate, FDR < 0.05 in Figure 2D(i)). In the case of astrocyte DEGs, we detected ~6000 up- and down-regulated HD-associated DEGs, which were decreased by A-ZFP and also by N-ZFP (Figure 2D(i)). In the case of neuronal HD DEGs, we detected effects of N-ZFP and lesser effects of A-ZFP (Figure 2D(i)). We imposed two additional criteria of a Log_2 fold-change (log_2FC) of >0.3 between R6/2 and NCAR, and a log_2FC >0.3 for enrichment in the IP fractions for astrocytes and neurons relative to bulk RNA-seq (Figure 2D(ii)). With these stringent criteria the total number of DEGs was decreased, but A-ZFP and N-ZFP still reduced the total HD-associated DEGs (Figure 2D(ii)). A-ZFP mostly showed a cell autonomous effect for restoration of astrocyte DEGs, whereas the N-ZFP, unexpectedly showed efficacy not only in restoration of neuronal DEGs, but also had a restorative impact on astrocyte DEGs (Figure 2D(ii)).

We used Volcano plots to show up- and down-regulated DEGs under the various conditions (Figure 2E). First, the data show astrocyte and neuron specific DEGs within the Delta-treated groups, which defines the HD “disease” condition (Figure 2E(i) and (iv)). Second, the data reveal changes to these HD DEGs in each cell type following expression of ZFPs in astrocytes or neurons. Namely, of the 2038 astrocyte DEGs, 748 (37%) were no longer differentially expressed after A-ZFP (Figure 2E(ii)). Similarly, of the neuronal 2393 DEGs, 1175 (49%) were no longer differentially expressed after N-ZFP (Figure 2E(vi)).

Thus, cell autonomous effects of mHTT rescue are greater for neurons than astrocytes. Third, of the 2393 neuronal DEGs, 367 (15%) were rescued by A-ZFP (Figure 2E(v)). In contrast, of the 2038 astrocyte DEGs, 1320 (64%) were rescued by N-ZFP (Figure 2E(iii)). Accordingly, mHTT in both astrocytes and neurons has non-cell autonomous consequences, but the greatest effect is that of mHTT in neurons impacting astrocytes. Whereas 15% of the neuronal DEGs were downstream of astrocyte dysfunction, 64% of astrocytic DEGs were downstream of neuronal dysfunction, implying that perhaps astrocytes are responding to greater neuronal dysfunction.

Mechanisms following cell autonomous and non-cell autonomous striatal mHTT lowering

We plotted the top 50 up- and down-regulated cell-specific HD DEGs from the Delta-treated groups (HD disease signature) along with the effect of A-ZFP or N-ZFP upon them for astrocytes and neurons (Figure 3A, B). From these graphs, HD DEGs were rescued by A-ZFP and N-ZFP, with the latter having a greater effect. We also performed Ingenuity Pathway Analysis (IPA) for the HD DEGs from astrocytes and neurons (Figure 3C, D). For astrocytes, the major altered pathways were related to fatty acid and cholesterol metabolism (Figure 3C). For the top pathway, super pathway of cholesterol biosynthesis, the top 16 genes were rescued by A-ZFP and N-ZFP (Figure 3C). For neurons, the core altered pathways were related to opioid signaling, calcium signaling, Gαq signaling, cAMP signaling, and synaptogenesis, which recalls past work [6,15,30]. For the top opioid signaling pathway, the top 16 genes were affected by A-ZFP and N-ZFP, and rescued very strongly by the latter (Figure 3D). These data define the major gene expression changes in HD, the molecular pathways altered in HD, and how mHTT lowering in neurons affected these parameters to a great degree.

We evaluated astrocyte HD DEGs from RNA-seq data to identify genes rescued by A-ZFP, N-ZFP or both and plotted the top 10 up- and down-regulated genes with heat maps (Figure 3E). Similar analyses were performed for the neuron enriched HD DEGs (Figure 3F). Next, we performed IPA using the genes rescued by A-ZFP in relation to those rescued by N-ZFP for astrocytes (748 rescued by A-ZFP, 1320 rescued by N-ZFP) and neurons (367 rescued by A-ZFP, 1175 rescued by N-ZFP), and determined overlap between the pathways for astrocytes and neurons, which was high (Figure 3G,H). These analyses define the major cell autonomous and non-cell autonomous effects of lowering mHTT in astrocytes and neurons for HD. Notably, the major pathways rescued in astrocytes were related to metabolism and cholesterol, whereas the major pathways in neurons were related to GPCRs, calcium, and cAMP signaling. Thus, our analyses show that the genes and pathways that were rescued by mHTT lowering represent reversal of changes associated with HD (Figure 3C,D; Figure 3G,H), emphasizing that presymptomatic mHTT lowering can prevent the development of subsequently expected HD-associated molecular signatures at symptomatic ages in mice.

Other HD gene signatures from human and mouse studies: assessing striatal ZFP effects

We found little evidence for uniquely A1 astrocytes [31] in HD [15] and no evidence of A-ZFP or N-ZFP affecting A1 marker genes in R6/2 mice (Figure S4C). These studies do not, however, rule out possible contributions of A1 marker genes to disease stages that we did not evaluate. We did find evidence of A-ZFP and N-ZFP reversing changes of astrocyte

DEGs identified previously in mouse models and post mortem human tissue [15] (Figure S4D), although at this stage the relationship of those genes to pathogenesis is unknown. We also mined single nuclei RNA-seq (snRNA-seq) data for R6/2 mice and postmortem human tissue [6] to determine how many of the HD-associated DEGs in astrocytes and D1/D2 MSNs from those studies overlapped with our data and how many were rescued by astrocyte- and neuron-specific mHTT lowering with ZFPs. We found significant rescue of HD DEGs in comparisons for R6/2 and human snRNA-seq data; effects of neuronal mHTT lowering were much greater than astrocytic mHTT lowering (Figure S5A–L).

Given the potential importance of astrocyte cholesterol metabolism for HD [32] (Figure 3C), we evaluated 89 genes involved in cholesterol biosynthesis and metabolism in our data (Delta, A-ZFP, N-ZFP), for zQ175 knock-in HD model mice [15], the allelic series of HD model mice with variable polyglutamine lengths [7], R6/2 and human snRNA-seq data [6], bulk RNA-seq data from human HD post mortem tissue [30], and microarray data from HD mouse models and human astrocytes derived from human embryonic stem cells or fetal striatal astrocytes expressing mHTT [33]. Consistent with Figure 3C, we found that disruption of cholesterol metabolism was a core feature of astrocytes in mouse models and in human data when DEGs were assessed with RNA-seq (Figure S6). However, the agreement was weaker in relation to studies in zQ175 mice and for astrocytes derived from human embryonic stem cells that used fluorescence activated cell sorting and microarrays [33] (Figure S6). Our evaluations suggest that dysfunction of astrocytic cholesterol metabolism is a core feature of HD that can be rescued by mHTT lowering.

We assessed 46 genes known to carry CAG repeats or to be downstream of genes that carry CAG repeats [14] in our A-ZFP and N-ZFP data for astrocytic and neuronal RNA-seq (Figure S7). Most were not detected with criteria for astrocyte and neuron enrichment (Figure 2D(ii)), but of those that were, we found suppression of *Nap1l3*, *Dach1*, and *Dnajc12* only in neurons following N-ZFP, and suppression of *Eid2b* in astrocytes following N-ZFP or A-ZFP (Figure S7). This was expected as *Nap1l3*, *Dach1*, and *Dnajc12* are comparatively depleted in astrocytes relative to input, whereas *Eid2b* is neither depleted nor enriched in astrocytes relative to the IP fraction (Figure S7). Overall, the analyses of cell type markers (Figure 1D,F, Figures S1–3), MDS (Figure 2C), and known off target genes repressed by ZFPs (Figure S7) suggests that our approach and analyses detected mainly astrocyte and neuronal gene expression and their alterations following ZFPs.

Whole-cell patch-clamp of MSNs following striatal mHTT lowering

We next performed patch-clamp electrophysiology experiments in brain slices following intrastriatal AAV microinjections to determine if the strong effect of N-ZFP on mHTT levels (Figure 1) and HD DEGs (Figures 2 and 3) was also associated with improved MSN function. We found that N-ZFP significantly, but subtly, improved excitability as measured by input-output curves (Figure S8A,B). N-ZFP also significantly restored the resting membrane potential, cell capacitance, membrane resistance, and Rheobase (Figure S8A–F). Furthermore, N-ZFP rescued the loss of spontaneous excitatory post synaptic currents (sEPSCs) associated with HD in R6/2 mice, with no effect on sEPSC amplitude (Figure

S8G–I). In contrast, astrocytic ZFPs did not improve these MSN electrophysiological properties (Figures S8J–R).

Molecular evaluations in zQ175 knock-in mice following striatal neuronal mHTT lowering

We performed a set of experiments with heterozygous zQ175 knock-in mice, which have a human Exon1 with an expanded CAG tract of ~190 CAGs knocked into the murine full length *Htt* gene [27]. ZFP administration will only repress the mHTT allele, with the resultant mice retaining murine unexpanded Htt at levels that would be comparable to the expected amount of WT Htt retained in a human setting, as the vast majority of HD patients carry only one affected allele. AAVs containing N-ZFP or N-Delta were microinjected intrastriatally at 6 months of age and neuron-specific and bulk RNA-seq was performed at 12 months (Figure S9A). The N-ZFPs reduced mHTT levels in Darpp32 positive neurons at 12 months by ~55% (Figure S10A,B). Our evaluations in 12 month old zQ175 mice showed that N-ZFPs were effective at reducing HD-associated DEGs and pathways in neuronal RNA-seq data (Figure S9B,C, S9H–J), that known astrocytic DEGs from zQ175 mice were also significantly rescued by N-ZFPs within bulk RNA-seq (Figure S9D–G), and that HD-associated changes in glia identified in human data and overlapping with zQ175 bulk RNA-seq data were also partially rescued (Figure S10C–L). These data support the findings from R6/2 mice, namely that N-ZFP produces cell autonomous neuronal benefits as well as non-cell autonomous effects in astrocytes. The degree of neuronal mHTT aggregate lowering and rescue of gene expression was lower in zQ175 mice than in R6/2 mice, which is unsurprising given that N-ZFP was administered when aggregate pathology was already underway.

Brain wide mHTT lowering with ZFP PHP.eB AAVs

We next assessed whether N-ZFP or A-ZFP, when delivered throughout the CNS, would ameliorate HD behavioral phenotypes. We packaged A-ZFP and N-ZFP into BBB-penetrant PHP.eBs [34] to deliver them or the Delta controls throughout the brain (Figure 4A–C) of R6/2 and NCAR mice positive for the Ly6a receptor gene required for these AAVs to cross the BBB [35] (Figure S11A). HA-tagged A-Delta, N-Delta, A-ZFP, and N-ZFPs were detected throughout the brain and their expression studied relative to mHTT (Figure 4D–G; Figure S11B–I). mHTT aggregate intensity for brain areas such as the cortex, striatum, and hippocampus suggested that A-ZFP and N-ZFP lowered mHTT levels relative to the Delta controls (Figure S11B–I), allowing detailed astrocyte and neuron specific evaluations for the striatum (Figure 4H–K). A-Delta and A-ZFP were expressed in ~60% of astrocytes, but in negligible neurons (Figure 4H). Relative to A-Delta, A-ZFP resulted in ~70% reduction of mHTT aggregates in S100β positive astrocytes, but not in neurons (Figure 4I). N-Delta and N-ZFP were expressed in ~90% of neurons, but in no astrocytes (Figure 4J). Relative to N-Delta, N-ZFP resulted in ~80% reduction of mHTT aggregates in NeuN positive neurons, but not in astrocytes (Figure 4K). PHP.eB-driven N-ZFP and A-ZFP expressed throughout the mouse brain and lowered mHTT levels cell-specifically in astrocytes and neurons to within 10% of each other (Figure 4).

HD mouse behaviors following brain wide astrocytic and neuronal mHTT lowering

We evaluated a range of motor and innate behaviors to determine if brain wide A-ZFP or N-ZFP expression produced beneficial effects. We found significant improvement for ambulation in the open field, hindlimb clasping, self-grooming, forelimb grip strength, rearing, gait (footprint length and width), and nesting behavior with N-ZFPs (Figure 5A–R). Hind limb clasping, which is a strong feature of R6/2 mice was completely rescued by N-ZFP. In contrast, A-ZFP produced subtle effects in many cases that did not reach significance, except for footprint width (Figure 5N). Importantly, the behavioral metrics were identical in the NCAR mice for Delta versus the cognate A-ZFP and N-ZFP, implying that any potential repression of the off-target repressed genes [14] were behaviorally inconsequential (Figure 5A–R). We summarized the behavioral data for each evaluation for A-ZFP and N-ZFP (Figure S12A,B) and found that A-ZFP produced modest 26% improvement of the overall aggregate z-score, but that N-ZFP improved HD mouse behavioral phenotypes by ~89% (Figure 5, Figure S12A–B). The most robust improvement in mouse behavior was nesting, which presumably reflects multiple domains of motor, affective, and cognitive function in mice. R6/2 mice were highly deficient in nesting behavior as indicated by the residual weight of the nesting material after a period in the home cage. However, R6/2 mice following N-ZFP had almost completely restored levels of nesting behavior compared to NCAR (Figure 5Q–R). The ZFPs were well tolerated in NCAR and R6/2 mice with no obvious deleterious effects. However, relative to the Delta group, R6/2 mice receiving N-ZFPs gained less weight as they aged (Figure S12C–F). We do not have an explanation for this effect of the N-ZFP on R6/2 mice.

Bulk tissue RNA-seq and proteomics following brain wide mHTT lowering

After PHP.eB AAV administration to lower mHTT in astrocytes or neurons, we used bulk tissue RNA-seq and proteomics with liquid chromatography tandem mass spectrometry (LC-MS/MS) to assess how A-ZFP and N-ZFP affected striatal gene and protein expression in relation to the Delta controls (Figure 6A,B). For the astrocytic experiments, we detected 6918 DEGs by RNA-seq of the bulk striatum between R6/2 and NCAR Delta groups (HD condition) and 2508 of these (i.e. 36%) were no longer DEGs in the R6/2 A-ZFP group (Figure 6A,C). This is concordant with the previous dataset following instrastriatal administration, where 37% rescue of the astrocytic DEG signature was noted (Figure 2E). For the neuronal experiments, we detected 9151 DEGs by RNA-seq of the bulk striatum between R6/2 and NCAR Delta groups (HD condition). Remarkably, 8802 of these (i.e. 96%) were no longer DEGs in the R6/2- treated N-ZFP group (Figure 6B,D). This was a higher rescue than following intrastriatally restricted administration of the N-ZFP and assessment of neuronal DEGs (49%, Figure 2E). This may suggest that transcriptional dysregulation of striatum may be driven partly by extra-striatal neuronal dysfunction, which was rescued by brain wide N-ZFP. The greater rescue by N-ZFPs of bulk striatal gene expression supports earlier findings that N-ZFP produces beneficial effects in other cell types such as astrocytes (Figure 2E).

We detected ~2800 proteins in each case for the Delta groups, A-ZFP, and N-ZFP (Figure S13A–B). For the astrocytic experiments, of the 882 significantly differentially expressed proteins (DEPs) between R6/2 and NCAR, 62% (548 DEPs) were recovered by A-ZFP

(Figure 6A,E). Conversely, for the neuronal experiments, of the 513 DEPs between R6/2 and NCAR, 89% (491 DEPs) were recovered by N-ZFP (Figure 6B,F). A greater effect of N-ZFP on HD-associated DEPs was also observed when the Delta groups were combined between astrocytic and neuronal studies (Figure S13G). These data support RNA-seq evaluations and show significant reversal of HD DEPs following mHTT lowering with ZFPs, with neuronal ZFP having the largest effect. The top 50 up- and down-regulated DEPs rescued by A-ZFP or N-ZFP are shown in Figure 6G–J; the top IPA pathways for the HD DEPs are shown in Figure S13C–F. We also performed scale-free STRING analyses to explore protein-protein interaction (PPI) hubs between the top 100 DEPs that were rescued by A-ZFP (Figure 6K) and N-ZFP (Figure 6L), respectively. The major PPI hubs for the astrocytic data were related to mitochondrial function and DNA binding, whereas those for the N-ZFP group were related to cAMP and DNA binding proteins.

Brain wide neuronal mHTT lowering: early intervention and lifespan analyses

Since N-ZFPs were highly effective at reversing HD-associated pathophysiology across a range of metrics in relation to A-ZFPs, we performed two additional sets of experiments to further test their utility. First, we administered the N-ZFPs at a later time point (7 weeks), assessed mouse behavior at 11 weeks, and compared the data to the early intervention 4 week time point (Figure 7). We measured improvement in HD-associated behaviors with late N-ZFP administration, which were significant for hindlimb clasping and nesting assays, but across all behaviors the rescue of behavior was ~37% (Figure 7A,B). This is lower than the ~89% improvement observed with the early interventions (Figure 7A,B). The finding that early interventions were more effective than later N-ZFP administration (Figure 7A,B) most likely reflects greater mHTT lowering by early N-ZFP (~80%; Figure 4K) *versus* later N-ZFP administration (~20%; Figure S14A–C). mHTT aggregates are already formed by 7 weeks of age in R6/2 mice, implying that ZFP-mediated mHTT lowering is most effective before aggregate formation.

Second, we performed survival analyses on the R6/2 mice with early N-ZFP administration. In these experiments, we used the nesting assay as a measure of improved behavior (Figure 7R). We found no effect of N-Delta or N-ZFP on NCAR mice in terms of the nesting assay or survival curve (Figure 7C), which suggests that these AAVs produced no noticeable off-target effects. The R6/2 mice receiving the N-Delta ZFP showed deterioration in the nesting assay between days 45 and 70, which was followed by demise and death by day 120 (Figure 7C). In contrast, the R6/2 mice that had received the N-ZFP were significantly improved in the nesting assay at day 45, i.e. ~2 weeks after AAV administration, continued to improve between days 45–70, and were stable until day 110 for the nesting assay at levels equal to NCAR mice (Figure 7C). Over the subsequent weeks, the performance of the mice in the nesting assay deteriorated and the mice began to die between days 110 and ~185, such that they were all dead by day 185 (Figure 7C). These data provide evidence that N-ZFPs significantly improved the survival of R6/2 mice by ~60 days and that this was associated with improved performance in the nesting assay.

Discussion

There are three main findings from this study. First, by assessing the consequences of lowering mHTT in astrocytes or neurons for HD pathophysiology at molecular, cellular, electrophysiological, and behavioral levels *in vivo*, we found that the major disease drivers were neurons, with astrocytes displaying significant loss of essential functions that are likely downstream of neuronal dysfunction. Second, we found that neuronal ZFPs resulted in profound neuron-specific mHTT lowering, rescue of HD behavioral phenotypes, and extension of lifespan when delivered throughout the CNS. Third, we provide evidence that targeting mHTT early in disease progression before aggregate pathology is established is more effective than later intervention. Our findings support further translational development of ZFPs for effective neuronal mHTT lowering throughout the CNS, and our data dissect the contributions of astrocytes and neurons to HD pathophysiology *in vivo*.

Limitations of the study

We assessed mHTT levels using IHC for the aggregated form of mutant HTT and by qPCR in relation to the wild type HTT; our findings should be interpreted with these considerations in mind. Another limitation of our study is that we evaluated the consequences of mHTT lowering in R6/2 mice at the ages of four and seven weeks at the time of ZFP administration, leading to the conclusion that neuronal pathophysiology was greater than that of astrocytes. In future studies, ZFPs could be administered earlier to explore cell-specific contributions to HD pathophysiology during postnatal development. Finally, the astrocyte and neuronal RNA-seq data for controls as well as R6/2 and zQ175 HD model mice enables evaluations of how astrocytes and neurons differ in these mouse models and suggests that the R6/2 model represents a rapidly developing form of the molecular pathophysiology seen in zQ175 mice, as previously shown by comparing R6/2 and Q150 mice [36]. Detailed comparisons of the mouse models were not within the scope of our study, but are now possible with the provided data. Our findings should not be over interpreted, and further studies are needed with additional models, with additional mHTT lowering strategies, perhaps with early time points, and with additional endpoint metrics in a variety of species.

HD mouse models and their limitations

The R6/2 mouse model is widely used in HD research, exhibiting highly consistent signatures of transcriptional dysregulation between knock-in full length mouse models and human HD postmortem tissue evaluations [6,7,36,37]. This includes concordance of core HD astrocytic signatures between R6/2 and the zQ175 HD mouse models and human astrocyte DEGs [15]. Additional similarities include (*i*) the development of mHTT oligomeric, proto-fibrillar, and fibrillar aggregates and inclusion bodies, (*ii*) alterations in key neurotransmitter systems, (*iii*) similar cortical and striatal metabolic disturbances, and (*iv*) related neurophysiological phenotypes. The advantages of the R6/2 model over full length knock-in mouse models for robust behavioral phenotyping is also well established and was a consideration in our studies.

As with all mouse models of human disease, there are caveats. For instance, it is widely acknowledged that no HD mouse model currently exists that fully replicates all aspects

of HD, the most notable omission being the lack of overt striatal cell loss, which has not been unambiguously identified in any HD mouse model, although volumetric atrophy is a core feature of most models, ascribed to cell shrinkage and neuropil degeneration [16,38]. That withstanding, one criticism levelled at the R6/2 model is that it does not encode the full length mHTT protein, i.e. that the HTT transgene only contains the promoter and exon 1 fragment of human HTT with ~120 CAG repeats inserted into the mouse genome. Interestingly, full length HTT is subject to extensive (mostly N-terminal) proteolytic processing and post-translational modification, and mHTT aggregation arises from N-terminal fragments of expanded mHTT between 50 – 150 kDa [39]. Of relevance here is the recent discovery that incomplete splicing of the first intronic sequence between Exon 1 and 2 of HTT leads to the generation of a polyadenylated mRNA encoding only the highly toxic and pro-aggregating protein product of exon-1. The generation of this differentially generated mRNA is CAG-length dependent, is present in all knock-in and transgenic full length mice with CAG lengths of 50 and above [40–43] and in juvenile-onset HD postmortem brain [42]. This points to a mechanism by which the inborn length of the CAG in humans, subsequently further expanded by somatic instability, leads to a shift in transcriptional processing from a full-length transcript to a highly pathogenic truncated exon-1 transcript [44]. Thus, it is emerging that the R6/2 model represents a valuable and relevant HD preclinical research model, allowing the establishment of causality between relevant exclusive Exon 1 protein driven pathology and HD symptoms, in short lived preclinical species such as mice that cannot generate sufficient CAG repeat expansions through somatic instability to study disease symptoms over their lifetime.

Neuronal and astrocytic contributions to HD pathophysiology

Astrocytes are increasingly implicated in brain disorders. However, astrocytic contributions relative to those of neurons towards pathophysiology remain largely unexplored directly *in vivo*. Our data showing that mHTT load within astrocytes was lower than in neurons are consistent with past work in HD mouse models and in post mortem human tissue for both HTT and mHTT [5,8,15]. We used ZFP-based genetic approaches [14] to lower mHTT levels cell-specifically and dissected how neurons and astrocytes contribute to HD pathophysiology in a severely presenting HD mouse model. With intra striatal and brain wide A-ZFP delivery, the astrocytic mHTT lowering was 70 and 70%, respectively. In comparison, the equivalent numbers for neuronal mHTT lowering by intra striatal and brain wide N-ZFPs were 95 and 80%, respectively. Thus, for our most comprehensive evaluations (marker expression, behavioral, transcriptomic, and proteomic data), the N-ZFPs and A-ZFPs were comparably effective at lowering mHTT to within ~10% of each other in their cognate cell type (80% versus 70%). Ideally, the mHTT lowering in each cell type would be 100% after cell-specific ZFP delivery, but we are aware of no genetic method to achieve such results with ZFPs in HD model mice (either viral or transgenic). Irrespectively, our data provide the metrics by which to judge future improvements in ZFPs for their ability to lower mHTT levels and their relation to beneficial effects with regards to HD pathophysiology in mice. Importantly, we did not observe obvious adverse effects of ZFPs, but we did observe that the R6/2 mice receiving N-ZFPs gained less weight in comparison to those receiving N-Delta control AAVs.

Our findings indicate that neurons show greater dysfunction than astrocytes in HD. Furthermore, our evaluations of cell autonomous and non-cell autonomous effects show that astrocytes likely respond to neuronal dysfunction. Thus, whereas 15% of HD-associated neuronal gene expression changes were downstream of astrocyte dysfunction, 64% of astrocytic changes were downstream of neuronal dysfunction. Astrocyte dysfunction likely precedes overt reactivity in HD, but our data suggest that major changes within astrocytes follow more consequential neuronal dysfunction. Consistent with these interpretations, in human HD tissue, there is loss of neurons at early neuropathological grades that is not accompanied by overtly reactive astrocytes [11,45]. Nonetheless, our findings do not rule out the possibility that astrogliosis contributes to pathology at later stages in the disease. Further studies are needed to identify the mechanism causing non-cell autonomous effects between astrocytes and neurons in the context of HD, but we speculate that cell-cell contacts ought to be explored as striatal astrocytes and neurons extensively interact and contain abundant cell adhesion molecules [46,47], some of which are disrupted in HD [7].

Translational implications

The major pathways that are altered in astrocytes in HD relate to supportive functions such as ion and neurotransmitter homeostasis and cholesterol metabolism [48–53]. Salvaging these essential astrocyte functions is likely to be beneficial with regards to pathology. Furthermore, pharmacologically targeting astrocytes to activate upstream regulators to promote protective functions in the context of HD is a viable strategy [29]. The major pathways in neurons that were rescued with ZFPs relate to those that were altered during disease progression (e.g. neuromodulation, synaptic, and intracellular signaling), which shows that appropriately timed and early presymptomatic mHTT lowering can offset subsequently expected molecular, cellular, and behavioral HD pathophysiology in mice. Our data with ZFPs show that early interventions are the most effective. However, this could be improved by combining them with strategies to clear preexisting mHTT aggregates at later ages. As far as we know, the extension of lifespan and behavioral improvements observed in R6/2 mice with peripherally administered N-ZFPs are greater than in previous translational studies and are promising from this perspective.

How do HTT ZFPs differentiate from other therapeutic HTT lowering approaches that are being trialed in the clinic? First, ZFPs have the potential to significantly abrogate mHTT production selectively where expressed, retaining full expression of unexpanded HTT from the unaffected allele [14]. The most advanced HTT lowering therapies that have entered clinical trials thus far are non-allele selective approaches to lower total HTT levels: an ASO therapy developed by Ionis/Roche (Tominersen), a virally delivered miRNA (Uniqure's AMT-130 [54,55]), and small molecule splicing modulators which are capable of causing nonsense mediated decay of HTT mRNA (Novartis' branaplam; [56] and PTC Therapeutics PTC-518 [57]). The only exception to this is Wave Therapeutics SNP-based mHTT-selective ASOs. Thus, mHTT selective lowering approaches such as ZFPs offer key potential advantages and may provide a higher therapeutic index. Second, as we have demonstrated, ZFPs can be targeted to specific cell types and therefore also have the potential to reduce safety liabilities regarding targeting other cells, which is not possible with non-cell specific delivery approaches such as ASOs. Third, ZFPs have the potential to be widely targeted

throughout the brain as we have shown. In Zeitler et al 2019, limited behavioral efficacy was evaluated following bilateral striatal injections to restrict ZFP expression to the striatum in R6/2 mice [14]. We show that with wider CNS mHTT lowering in R6/2 mice, behavioral phenotype ameliorations were much clearer. Further, we provide evidence that rescue of striatal transcriptional dysregulation was also enhanced when neuronal ZFPs were delivered throughout the CNS, suggestive that some of the striatal molecular pathology could be driven by extrastriatal dysfunctions. Furthermore, the significant improvement in disease-related phenotypes we report by delivering ZFPs to the brain with PHP.eB AAVs imply that whole body approaches may not be needed. This is important, because mHTT is expressed throughout the body and knowing that significant improvement can occur by exclusively targeting the CNS is critical to know. Fourth, ZFPs have the potential to be delivered (potentially just once) by systemic routes via AAVs that can cross the BBB, whereas the majority of clinical ASOs must be delivered repeatedly by intrathecal lumbar puncture to maintain efficacy. Although speculative for human HD adaptation at this point, a potentially once only treatment paradigm to correct disease course portends an attractive potential therapeutic candidate.

It is not possible to predict clinical success for humans from studies in mice alone, but our findings support translational refinement and development of ZFPs for neuronal mHTT lowering, together with pharmacological and cell replacement strategies to restore astrocytic homeostatic support for HD [10,29,58]. Furthermore, our approaches and data provide a basis to dissect the relative contributions of astrocytes and neurons to other neurodegenerative diseases where both cell types have been implicated for over a century.

STAR METHODS

RESOURCE AVAILABILITY

Lead Contact: Baljit S. Khakh (bkhakh@mednet.ucla.edu)

Materials availability: AAV5 *hSyn1* Rpl22HA plasmid is available from Addgene (ID #111811). The vectors incorporating Sangamo Biosciences / Takeda Inc mHTT zinc finger repressor proteins ZFP-30645 and ZFP-DBD were made by the Khakh lab. The original plasmids were obtained via CHDI Foundation under the terms of a Use Agreement by and between CHDI Foundation and Sangamo Biosciences. Requests for these plasmids should be made directly to CHDI Foundation (info@CHDIFoundation.org) with ZFP in the subject line.

Data and code availability:

- RNA-seq data have been deposited at the Gene Expression Omnibus repository and are publicly available as of the date of publication. Accession numbers are listed in the key resources table. Proteomic data have been deposited at PRIDE and are publicly available as of the date of publication. Accession numbers are listed in the key resources table.
- This paper does not report original code.

- Any additional information required to reanalyze the data reported in this paper is available from the lead contact upon request.

EXPERIMENTAL MODEL AND SUBJECT DETAILS

All animal experiments were conducted in accordance with the National Institute of Health Guide for the Care and Use of Laboratory Animals and were approved by the Chancellor's Animal Research Committee at the University of California, Los Angeles. As per policy, mice were housed in vivarium holding rooms managed by the Division of Laboratory Animal Medicine at University of California, Los Angeles (UCLA) with a 12 h light/dark cycle and *ad libitum* access to food and water. All animals were healthy with no obvious behavioral phenotype at the start of the experiments other than those expected in R6/2 mice, were not involved in previous studies, and were sacrificed during the light cycle. All R6/2 mice we used for experiments by 11 weeks. Only male mice were used in the experiments to reduce the potential effect of differences in transcriptome [15] and phenotype [59,60] between male and female HD model mice. Mice were assigned randomly to the experiments based on the genotype. Data for experiments were collected from adult mice (8–13 weeks old). For the PHP.eB AAV experiments, we genotyped for the permissive Ly6a variant in R6/2 and NCAR mice, because the PHP.eB AAVs are brain penetrant in mice that express this receptor for the PHP.eB capsid [35]. For such genotyping, tail-tip DNA was amplified using either C57insF (5'-CTGGAATTAGGAATGGTTGTGTG-3') and C57insR (5'-TTGTTCTTTACTTTCCTTGTTTGAGAAT-3') or CBAinsF2 (5'-TAGGAATGGTTGTAAACCAGG) and CBAinsR2 (5'-CCTCCATTGGGAACTGCTG) primers and recommended cycling conditions as described previously [35].

Mouse models—Wild-type C57BL/6NTac mice were generated from in house breeding colonies or purchased from Taconic Biosciences. R6/2 and non-carrier (NCAR) control mice at 4–5 weeks of age were purchased from the Jackson Laboratory (Strain B6CBA-Tg (HDexon1) 62Gpb/3J; JAX #006494); the R6/2 mice had an average CAG length of 120. Heterozygous zQ175 and wild-type (WT) control mice at 5–6 months of age were purchased from the Jackson Laboratory (Strain B6J.129S1-*Htt*^{tm1Mfc}/190ChdiJ; JAX #027410) with average CAG length of 190.

METHOD DETAILS

Cloning and adeno-associated virus (AAV) production—Adeno-associated viruses were prepared using standard methods. Briefly, ribosomal protein gene Rpl22 with three HA tags (Rpl22-HA) was amplified from a previously published astrocytic RiboTag plasmid (Addgene #111811). Rpl22-HA was then cloned into pZac2.1 containing the neuron specific promoter human synapsin-1 using restriction digestion (*XhoI* and *XbaI*) and the In-fusion® kit (Takara Bio). After sequencing, the resulting plasmid (pZac2.1-*hSyn1*-Rpl22-HA-WPRE-SV40) was sent to the UPenn Vector Core at the University of Pennsylvania for AAV serotype-5 production. The AAV concentration was 2.1×10^{13} genome copies/ml (GC/ml). Virus plasmids have been deposited at Addgene in the Khakh laboratory repository for free distribution (http://www.addgene.org/Baljit_Khakh). Sangamo Bioscience zinc finger repressor protein plasmids ZFP-30645 and DNA binding deleted control plasmid ZFP-DBD (nbZFP) were obtained via CHDI Foundation, under terms

of a Use Agreement between CHDI and Sangamo Biosciences. These were re-cloned to make pZac2.1-*GfaABC$_1$D*-ZFPDelta-HA-P2A-TdTomato-WPRE (A-Delta) and pZac2.1-*GfaABC$_1$D*-ZFP30645-HA-P2A-TdTomato-WPRE (A-ZFP) plasmids as reported [15]. These constructs were modified to replace the *GfaABC$_1$D* promoter with the neuron specific promoter, human synapsin-1. The resulting plasmids, pZac2.1-*hSyn1*-ZFPDelta-HA-P2A-TdTomato-WPRE (N-Delta) and pZac2.1-*hSyn1*-ZFP30645-HA-P2A-TdTomato-WPRE (N-ZFP) were sequenced and sent to Virovek (Hayward, CA) for AAV serotype-5 production. The AAV concentration was 2.1×10^{13} GC/ml. Note that in these constructs, slightly lower expression of genes 3' to the P2A sequence (i.e. tdTomato) relative to the 5' ZFP and Delta-ZFP from the same construct is expected due to ribosome fall-off of the transcript in some instances when P2A sequences are used.

Stereotaxic microinjections of adeno-associated viruses—Stereotaxic injections into the mouse striatum were performed using standard procedures. NCAR or R6/2 mice (4–5 weeks old) and zQ175 or WT mice (6 month) were used for surgeries in accordance with institutional guidelines. All surgical procedures were conducted under general anesthesia using continuous isoflurane (induction at 5%, maintenance at 1–2.5% vol/vol). Depth of anesthesia was monitored continuously and adjusted when necessary. Following induction of anesthesia, the mice were fitted into a stereotaxic frame with their heads secured by blunt ear bars and their noses placed into an anesthesia and ventilation system (David Kopf Instruments). Mice were administered 0.1 mg/kg of buprenorphine (Buprenex, 0.1 mg/ml) subcutaneously before surgery. The surgical incision site was then cleaned three times with 10% povidone iodine and 70% ethanol (vol/vol). Skin incisions were made, followed by craniotomies of 2–3 mm in diameter above the left frontal cortex using a small steel burr (Fine Science Tools) powered by a high-speed drill (K.1070, Foredom). Saline (0.9%) was applied onto the skull to reduce heating caused by drilling. Uni- or bi-lateral viral injections were carried out by using a stereotaxic apparatus (David Kopf Instruments) to guide the placement of beveled glass pipettes (1B100-4, World Precision Instruments). To inject in the striatum, the coordinates were 1 mm anterior to bregma, 2 mm lateral to midline, and 2.4 mm deep from the pial surface. AAV was injected by using a syringe pump (Pump11 PicoPlus Elite, Harvard Apparatus). Glass pipettes were left in place for at least 10 min prior to slow withdrawal. Surgical wounds were closed with external 5–0 nylon sutures. Following surgery, animals recovered overnight in cages placed partially on a low-voltage heating pad. Buprenorphine was administered two times per day for up to 2 days after surgery. In addition, trimethoprim sulfamethoxazole was provided in food to the mice for 2 weeks. Virus injected mice were euthanized six to seven weeks post-surgery for RNA extraction, live slice studies or perfused for immunohistochemistry. Four experimental conditions used for the RNA-seq experiments were as follows. First, 0.7 µl of AAV2/5-A-Rpl22-HA [*GfaABC$_1$D*-Rpl22-HA (2.1×10^{13} GC/ml)] with either 0.9 µl AAV2/5-A-Delta [*GfaABC$_1$D*-ZFPDeltaDBD-HA-TdTomato-WPRE (2.1×10^{13} GC/ml)] or 0.9 µl AAV2/5-A-ZFP [*GfaABC$_1$D*-ZFP30645-HA-tdTomato-WPRE (2.1×10^{13} GC/ml)]. Second, 0.7 µl AAV5-N-Rpl22-HA [*hSyn1*-Rpl22-HA-WPRE (2.1×10^{13} GC/ml)] with either 0.9 µl of AAV5-N-Delta [*hSyn1*-ZFPDeltaDBD-HA-TdTomato-WPRE (2.00×10^{13} GC/ml) or 0.9 µl of AAV5-N-ZFP [*hSyn1*-ZFP30645-HA-tdTomato-WPRE (2.03×10^{13} GC/ml)]. Third, 0.7 µl AAV5-N-Rpl22-HA [*hSyn1*-Rpl22-HA-WPRE (2.1×10^{13} GC/ml)] with either 0.9 µl

of AAV2/5-A-Delta [*GfaABC$_1$D*-ZFPDeltaDBD-HA-TdTomato-WPRE (2.1×10^{13} GC/ml) or 0.9 μl of AAV2/5-A-ZFP [*GfaABC$_1$D*-ZFP30645-HA-tdTomato-WPRE (2.1×10^{13} GC/ml)]. Fourth, 0.7 μl of AAV2/5-A-Rpl22-HA [*GfaABC$_1$D*-Rpl22-HA (2.1×10^{13} GC/ml)] with either 0.9 μl AAV5-N-Delta [*hSyn1*-ZFPDeltaDBD-HA-TdTomato-WPRE (2.00×10^{13} GC/ml) or 0.9 μl of AAV5-N-ZFP [*hSyn1*-ZFP30645-HA-tdTomato-WPRE (2.03×10^{13} GC/ml)].

Tissue preparation and immunohistochemistry—Mice were perfused intracardially using 0.1 M PBS for 2 min, followed by formalin for 10 min. Brains were extracted and submerged in formalin overnight. Next day, brains were washed once with 0.1 M PBS and transferred to 30% sucrose solution in 0.1 M PBS and kept at 4°C until saturated and sunk to the bottom of the tubes. Brains were then embedded in the OCT Tissue Tek medium (VWR #25608-930) compound and coronal sections (40 μm) or sagittal sections (60 μm) were prepared using a cryostat microtome (Leica). The sections were then kept in 0.05 M PBS, 250 mM sucrose, 7 mM MgCl2, 50% Glycerol at −20°C until further use. For immunohistochemistry, sections were washed once in 0.1 M PBS for 10 min, once in 0.1 M PBS with 0.2 % Triton® X-100, and then incubated in blocking solution containing 10% NGS in 0.1 M PBS with 0.2% Triton® X-100 for 1 hour at room temperature with constant shaking. For mHTT immunostaining, antigen retrieval was performed by incubating the slices in 10% formic acid for 10 min. Formic acid was washed out three times in 0.1 M PBS. Slices were then incubated in blocking solution as described above. Sections were subsequently incubated in primary antibodies diluted in 5% NGS in 0.1 M PBS with 0.2% Triton® X-100 solution overnight at 4°C with constant shaking. The following primary antibodies were used: mouse anti-HA (1:1000; Biolegend 901514), rabbit anti-S100β (1:1000, Abcam ab41548), chicken anti-S100β (1:500; Synaptic Systems 287006), rabbit anti-NeuN (1:2000; Cell Signaling D3S3I), guinea pig anti-NeuN (1:500; Synaptic Systems 266004), rabbit anti-DARPP-32 (1:200 Abcam ab40801), chicken anti-GFAP (1:1000; Abcam ab4674), rabbit anti-RFP (1:1000; Rockland antibodies and assays 600-401-379) mouse anti-mHTT (1:400 Millipore MAB5492, clone 2B4), mouse anti-mHTT (1:400 Millipore MAB5374, clone mEM48). Next day the sections were washed three times in 0.1 M PBS with 0.2 % Triton® X-100 for 10 min each before incubation at room temperature for 2 hr with secondary antibodies diluted in blocking solution. The following Alexa conjugated (Molecular Probes) secondary antibodies were used: goat anti-mouse 405, 546 and 647 (1:1000), goat anti-rabbit 488, 546 and 647 (1:1000), goat anti-chicken 488 (1:1000). The sections were rinsed two times in 0.1 M PBS with 0.2 % Triton® X-100 for 10 min each, and once in 0.1 M PBS for 10 min. The sections were incubated in DAPI 140 ng/μl in 0.1 M PBS for 10 min, rinsed once in 0.1 M PBS for 10 min and mounted on microscope slides in Fluoromount-G. Fluorescent images were taken using UplanSApo 20X or UPLXAPO 10X and UPlanFL 40X, UPLFLN 40X, UPLXAPO 60X oil immersion objective lens on an upright confocal laser-scanning microscope (FV1000 and FV3000; Olympus). We used the 458 nm line of an Argon to excite DAPI, with the intensity adjusted to 2–8% of the maximum output (0.6 mW). Alexa 488 was excited by an Argon laser, with the intensity adjusted to 2–6% of the maximum output (3.5 mW). Alexa 546 was excited by the 543 nm laser line of the HeNe-G laser at 20–25% of the maximum output (1 mW). Alexa 647 was excited by laser line of the HeNe-R laser at

5–10% of the maximum output (3.5 mW). The settings were the same for each experiment. Images represent maximum intensity projections of optical sections with a step size of 0.5 or 1.0 μm and depth of 10–15 μm. The images were analyzed for colocalization or mHTT lowering from 3–4 mice and with 6–16 fields of view in each group at either 40x or 60x magnification. Each image was acquired at 16-bit depth and the brightest pixels were less than 10% of the brightest possible value of 2^16; this was true also after the z-projection in ImageJ. The person doing the imaging was not blinded to the experiments.

Gene expression analysis using qPCR—RNA-seq cannot be used to reliably discriminate between mHTT and HTT in our data. RNAseq produces short reads (50 to 300 bp) from mRNA, which can be used to quantify gene transcription through mapping of the short sequencing reads. Due to the large size of the HTT mRNA (13.47 kb and 67 exons), poly-A primed RNA-seq protocols yield negligible coverage of 5' exons. As CAG expansions of HTT leading to HD are in the first 5'exon, differentiating mHTT from HTT using RNA-seq is not possible with the methods we employed. Furthermore, loss of any mHTT expression following ZFPs would not be detected quantifiably in overall HTT mRNA expression levels by RNA-seq. For these reasons, we assessed mHTT and HTT by IHC and qPCR. Thus, astrocytic and neuronal immunoprecipitated RNA was extracted using RNeasy Plus Micro Kit (QIAGEN #74034). Complementary DNA was generated using High-capacity cDNA reverse transcription kits (Thermo Fisher Scientific). Reverse transcriptase quantitative (qPCR) was performed using PrimeTime® Gene Expression Master Mix (IDT, Inc.) and LightCycler 96 real-time PCR machine (Roche). The following pre-designed qPCR primer/probe assays for gene expression analysis were ordered (IDT, Inc.): *Atp5b* (Mm.PT.53a.17279462), *HTT* (Mm.PT.58.6953479). Mutant *Htt* mRNA in R6/2 mice was detected using the following primer/probe set: Forward primer: CGCAGGCTGCAGGGTTAC, Reverse primer: GCTGCACCGACCGTGAGT, Probe: CAGCTCCCTGTCCCGGCGG. For each sample, 10 μl qPCR reactions were set up as follows: 5 μl PrimeTime® Gene Expression Master Mix (IDT, Inc.), 1 μl of 10× primer/probe Master mix (final concentration 0.5 μM for each primer and 0.25 μM for the probe), 2 μl H_2O and 2 μl of cDNA sample. Thermal cycling conditions were as follows: (1) 95 °C for 3 min; (2) 95 °C for 30 s; (3) 66 °C for 30 s; (4) 72 °C for 90 s; (5) plate read, repeat steps 2–5, 35 times; (6) end. Expression was calculated based on Ct values of the genes of interest relative to Atp5b using the following formula: 2-ΔCt.

RNA-seq of mouse striatal astrocyte and neuron transcriptomes using RiboTag method—NCAR and R6/2 male mice (4 week old) were bilaterally injected in the striatum with astrocytic RiboTag (AAV2/5-*GfaABC$_1$D*-Rpl22-HA) or neuronal RiboTag (AAV2/5-*hSyn1*-Rpl22-HA) in conjunction with astrocytic ZFPs (AAV2/5-*GfaABC$_1$D*-ZFPDeltaDBD-HA-TdTomato-WPRE or AAV2/5-*GfaABC$_1$D*-ZFP30645-HA-TdTomato-WPRE) or neuronal ZFPs (AAV5-*hSyn1*-ZFPDeltaDBD-HA-P2A-TdTomato-WPRE or AAV5-*hSyn1*-ZFP30645-HA-P2A-TdTomato-WPRE). RNA was immunoprecipitated (IP) from astrocytes or neurons at 11-week-old. zQ175 and WT mice were bilaterally injected with neuronal RiboTag in the striatum and the RNA was immunoprecipitated at 12 month-old. Briefly, freshly dissected striatum tissues were collected and individually homogenized in 1 ml of homogenization buffer (50 mM Tris pH 7.4, 100 mM KCl, 12 mM MgCl2,

1% NP-40, 1 mM Dithiothreitol (DTT), 1X Protease inhibitors, 200 U/ml RNAsin, 100 μg/ml Cyclohexamide, 1 mg/ml Heparin). RNA was extracted from 20% of cleared lysate as Input (200 μl). The remaining lysate (800 μl) was incubated with 5 μl of mouse anti-HA antibody (Biolegend #901514) with rocking for 4 hours at 4°C followed by addition of 200 μl of magnetic beads (Pierce #88803) and overnight incubation with rocking at 4°C. The beads were washed three times in high salt solution (50 mM Tris pH 7.4, 300 mM KCl, 12 mM MgCl2, 1% NP-40, 1 mM Dithiothreitol (DTT), 100 μg/ml Cyclohexamide). RNA was purified from the IP and corresponding Input samples (RNeasy Plus Micro QIAGEN #74034). RNA concentration and quality were assessed with Agilent 2100 Bioanalyzer. RNA samples with RNA integrity number (RIN) greater than seven (mean RIN 8.2) were processed with Ribo-Zero Gold kit (Epicentre, WI) to remove ribosomal RNA. Sequencing libraries were prepared using Illumina TruSeq RNA sample prep kit following manufacturer's protocol. After library preparation, amplified double-stranded cDNA was fragmented into 125 bp (Covaris-S2, Woburn, MA) DNA fragments, which were (200 ng) end-repaired to generate blunt ends with 5'- phosphates and 3'- hydroxyls and adapters ligated. The purified cDNA library products were evaluated using the Agilent Bioanalyzer (Santa Rosa, CA) and diluted to 10 nM for cluster generation in situ on the HiSeq paired-end flow cell using the CBot automated cluster generation system. We analyzed five sequencing experiments with RiboTag AAVs. In the first sequencing experiment, NCAR and R6/2 mice were injected with astrocytic RiboTag AAVs along with astrocytic ZFP AAVs (A-Delta or A-ZFP) in the striatum; as previously reported[15] and analyzed here together with the other experimental groups below. In the second sequencing experiment, NCAR and R6/2 mice were injected with neuronal RiboTag AAVs along with astrocytic ZFP AAVs (A-Delta or A-ZFP) in the striatum. In the third sequencing experiment, NCAR and R6/2 mice were injected with neuronal RiboTag AAVs along with neuronal ZFP AAVs (N-Delta or N-ZFP) in the striatum. In the fourth sequencing experiment, NCAR and R6/2 mice were injected with astrocytic RiboTag AAVs along with neuronal ZFP AAVs (N-Delta or N-ZFP) in the striatum. In the fifth sequencing experiment, WT and zQ175 mice were injected with neuronal RiboTag AAVs along with neuronal ZFP AAVs (N-Delta or N-ZFP) in the striatum. Samples in each experiment were multiplexed into a single pool to avoid batch effects and 69 bp-paired-end sequencing was performed using an Illumina HiSeq 4000 sequencer (Illumina, San Diego, CA). A yield between 51 and 108 million reads was obtained per sample. Quality control was performed on base qualities and nucleotide composition of sequences. Reads were aligned to the mouse mm10 reference genome using the STAR spliced read aligner with default parameters. Fragment counts were derived using HT-seq program with mouse mm10 refSeq (refFlat table) as a reference and used as a basis for the quantification of gene expression. Only uniquely mapped reads were used for subsequent analyses. Additional QC was performed after the alignment to examine: the degree of mismatch rate, mapping rate to the whole genome, repeats, chromosomes, key transcriptomic regions (exons, introns, UTRs, genes), insert sizes, AT/GC dropout, transcript coverage and GC bias. Between 75 and 94% (average 87.6%) of the reads mapped uniquely to the mouse genome. Batch effects were corrected by Bioconductor R package RUVr using the first 4 principal components of residuals. Differential expression analysis was conducted with R-project and the Bioconductor packages voom, EdgeR, and limma.

RNA-seq data has been deposited within the Gene Expression Omnibus (GEO) repository (www.ncbi.nlm.nih.gov/geo), accession number GSE189647.

Retro-orbital sinus injection of PHP.eB AAVs—PHP.eB serotype AAVs were prepared at UMASS Medical School Gene Therapy Center and Vector Core. Viruses were injected at 1×10^{12} genome copies per mouse diluted in saline solution to a volume of 70 µl. AAV-PHP.eB-A-Delta [*GfaABC$_1$D*-ZFPDeltaDBD-HA-TdTomato-WPRE (2.5×10^{13} GC/ml)], AAV-PHP.eB-A-ZFP [*GfaABC$_1$D*-ZFP30645-HA-tdTomato-WPRE (1.7×10^{13} GC/ml)], AAV-PHP.eB-N-Delta [*hSyn1*-ZFPDeltaDBD-HA-TdTomato-WPRE (2.0×10^{13} GC/ml)], AAV-PHP.eB-N-ZFP [*hSyn1*-ZFP30645-HA-tdTomato-WPRE (2.1×10^{13} GC/ml)]. NCAR or R6/2 (4–5 weeks old) were used for injections in accordance with institutional guidelines. Briefly, mice were anesthetized in the induction chamber using 5% vol/vol isoflurane and depth of anesthesia was monitored continuously. An insulin syringe (BD insulin syringes with BD Ultra-Fine needle, 31G) was loaded with diluted virus and bubbles in the syringe were removed. The anesthetized mouse was placed on the heated pad in the prone position with the head facing the dominant hand. A nose cone was used to maintain anesthesia at 1.25–2.5% vol/vol isoflurane. After assessing the depth of anesthesia using pedal (toe pinch) reflex, the index finger and thumb on the non-dominant hand was used to slightly protrude the eye from the socket. The needle was injected with the dominant hand, bevel down to 30–45° in the retro-orbital sinus situated behind the globe of the eye. Virus was slowly released into the retro-orbital sinus and the needle was removed gently. Following viral injection, 1–2 drops of proparacaine solution was applied to the corneal surface for local analgesia. The mouse was placed in the clean cage and monitored for recovery. Mice weights were measured weekly after the injection until the experimental endpoint.

Behavioral assessments—All the behavioral assessments were carried out during the light cycle between 10:00 am and 6:00 pm. Experimental mice were transferred to the testing facility at least 30 min before the start of the testing and allowed to acclimatize to the environment to reduce stress during assessments. Facility was maintained at constant temperature and humidity of 23 ± 2°C and 55 ± 5%, respectively. Background noise was maintained at 65 ± 2 dB by using white noise generator (San Diego Instruments).

Open field test: After 30 min of habituation, mice were allowed to freely explore the open field chamber (l = 28 cm, w = 28 cm, h = 19 cm) for 10 min. The camera (Logitech) fitted on the top of the enclosed chamber was used to record the locomotor activity which was analyzed using AnyMaze video tracking software (Stoelting).

Hind limb clasping: Each mouse was suspended by holding the tail at a height of approximately 10 inches above the home cage. Time taken (in seconds) by the mouse to move both forelimbs close to the body and for both paws to clasp was recorded. Maximum allotted time for clasping was 60 s and the mice that did not clasp in that time were given a data value of 60 s. Mice that visibly clasped in under 60 s were immediately lowered into the home cage to avoid any distress.

Self-grooming behavior: Mice were placed individually into plastic cylinders (15 cm in diameter and 35 cm tall) and allowed to habituate for 20 min. Self-grooming behavior was recorded for 10 min using a camera placed adjacent to the cylinder. Videos were analyzed by a person blinded to the experiment to assess the cumulative time spent engaged in self-grooming behavior, which included paw licking, unilateral and bilateral strokes around the nose, mouth, face, paw movements over the head and behind ears, body fur licking, body scratching with hind paws, tail licking, and genital cleaning. Self-grooming microstructure was not assessed. Frequency of rearing was also assessed for each mouse by the same person blinded to the experiment.

Forelimb grip strength: Forelimb strength was measured using a customized grip strength meter (Columbia instruments) with an adjustable wire mesh grip designed for mice. Both the grip strength meter and the mesh grip were positioned horizontally. Each mouse was held by the base of the tail and lowered to grasp the mesh with both forelimbs. A steady horizontal force was then applied to extend the mouse away from the mesh until it relinquished its grip on the mesh. Maximum pulling force required to separate the mouse from the mesh grip was recorded by the meter. Each mouse was tested in five trials with a 5 min inter trial interval and average maximum pulling force (per mouse) was used to assess grip strength.

Nesting assay: Mice were provided with pressed cotton squares (Nestlets) in the home cage. Unshredded nestlets free of loose material were weighed at the end of 72 hour. If there was no Nestlet (i.e. it was fully shredded), then a value of 0 g was assigned.

Footprint test: A 1 m long runway (8 cm wide) was lined with paper. Each mouse with hind paws painted with non-toxic black ink was placed at an open end of the runway and allowed to walk to the other end. For the gait analysis, stride length and width were measured and averaged for both left and right hindlimbs over five consecutive steps.

Behavioral z-scores: For each behavioral assay, the mean (M) and standard deviation (SD) for the entire population was calculated from the individual values (I) in all four experimental groups for astrocytic and neuronal ZFPs. We then calculated the z-scores as, $z = (I - M)/SD$. Average z-scores for each experimental group were calculated from the individual z-scores and plotted using a color scale in the figures.

Incidentally, cell loss does not occur in the R6/2 model and consistent with this, we found no evidence that either A-ZFP or N-ZFP increased the numbers of astrocytes or neurons relative to controls, respectively in R6/2 mice (Supplementary Table 1).

Striatal bulk RNA sequencing—NCAR and R6/2 male mice (4 week old) were retro-orbitally injected with AAV-PHP.eB-A-Delta [*GfaABC$_1$D*-ZFPDeltaDBD-HA-TdTomato-WPRE (2.5×10^{13} GC/ml)], AAV-PHP.eB-A-ZFP [*GfaABC$_1$D*-ZFP30645-HA-tdTomato-WPRE (1.7×10^{13} GC/ml)], AAV-PHP.eB-N-Delta [*hSyn1*-ZFPDeltaDBD-HA-TdTomato-WPRE (2.0×10^{13} GC/ml)], AAV-PHP.eB-N-ZFP [*hSyn1*-ZFP30645-HA-tdTomato-WPRE (2.1×10^{13} GC/ml)] at 1×10^{12} genome copies per mouse. Striata from R6/2 and NCAR mice were dissected and lysed in 350 μl lysis buffer. RNA was extracted using RNeasy Plus mini kit (Qiagen, 74134) following manufacturer's protocol. RNA concentration and

quality were assessed with Agilent 2100 Bioanalyzer. RNA samples with RNA integrity number (RIN) greater than seven were processed with Ribo-Zero Gold kit (Epicentre, WI) to remove ribosomal RNA. Sequencing libraries were prepared using Illumina TruSeq Stranded RNA sample prep kit following manufacturer's protocol. After library preparation, amplified double-stranded cDNA was fragmented into 125 bp (Covaris-S2, Woburn, MA) DNA fragments, which were (200 ng) end-repaired to generate blunt ends with 5'- phosphates and 3'- hydroxyls and adapters ligated. The purified cDNA library products were evaluated using the Agilent Bioanalyzer (Santa Rosa, CA) and diluted to 10 nM for cluster generation in situ on the HiSeq paired-end flow cell using the CBot automated cluster generation system. Samples in each experiment were multiplexed into a single pool to avoid batch effects and 69 bp-paired-end sequencing was performed using an Illumina NovaSeq 6000 sequencer (Illumina, San Diego, CA). A yield between 70 and 142 million reads was obtained per sample. Quality control was performed on base qualities and nucleotide composition of sequences. Reads were aligned to the mouse mm10 reference genome using the STAR spliced read aligner with default parameters and fragment counts derived using HTS-seq program. Additional QC was performed after the alignment to examine: the degree of mismatch rate, mapping rate to the whole genome, repeats, chromosomes, key transcriptomic regions (exons, introns, UTRs, genes), insert sizes, AT/GC dropout, transcript coverage and GC bias. Between 75 and 94% (average 87.6%) of the reads mapped uniquely to the mouse genome. Total counts of read fragments aligned to candidate gene regions were derived using HTSeq program (www.huber.embl.de/users/anders/HTSeq/doc/overview.html) with mouse mm10 refSeq (refFlat table) as a reference and used as a basis for the quantification of gene expression. Only uniquely mapped reads were used for subsequent analyses. Differential expression analysis was conducted with R-project and the Bioconductor package limma-voom. RNA-seq data has been deposited within the Gene Expression Omnibus (GEO) repository (www.ncbi.nlm.nih.gov/geo), accession number GSE211891.

Bulk proteomics and analysis using mass spectrometry—Striata from 11 week old R6/2 and NCAR mice were lysed in 200 µl lysis buffer (8 M urea, 50 mM Tris-HCl pH 8.2, 75 mM NaCl, 5 mM EDTA, 5 mM EGTA, 10 mM sodium pyrophosphate, protease inhibitor cocktail) as described previously [7]. Tissues were homogenized and extracts were sonicated. Samples were centrifuged at >14,000g, 4°C for 20 min to remove tissue/cell debris. The supernatants were collected and stored at 4°C until ready for further processing.

Protein samples were subjected to reduction using 5 mM Tris (2-carboxyethyl) phosphine for 30 min, alkylated by 10 mM iodoacetamide for another 30 min. SP3 protein cleanup and multi enzymatic digestion overnight at 37°C were successfully performed using paramagnetic bead–based workflow as described elsewhere [61] where and trypsin/LysC, respectively. The peptide pellet was reconstituted in 5% formic acid before analysis by liquid chromatography-tandem mass spectrometry (LC-MS/MS).

Tryptic peptide mixtures were loaded onto a 25 cm long, 75 µm inner diameter fused-silica capillary, packed in-house with bulk 1.9 µM ReproSil-Pur beads with 120 Å pores. Peptides were analyzed using a 140 min water-acetonitrile gradient delivered by a Dionex Ultimate 3000 UHPLC (Thermo Fisher Scientific) operated initially at 400 nL/min flow rate with 1%

buffer B (acetonitrile solution with 3% DMSO and 0.1% formic acid) and 99% buffer A (water solution with 3% DMSO and 0.1% formic acid). Buffer B was increased to 6% over 5 min at which time the flow rate was reduced to 200 nl/min. A linear gradient from 6–28% B was applied to the column over the course of 123 min. The linear gradient of buffer B was then further increased to 28–35% for 8 min followed by a rapid ramp-up to 85% for column washing. Eluted peptides were ionized via a Nimbus electrospray ionization source (Phoenix S&T) by application of a distal voltage of 2.2 kV.

The spectra were collected using data dependent acquisition on Orbitrap Fusion Lumos Tribrid mass spectrometer (Thermo Fisher Scientific) with an MS1 resolution of 120,000 followed by sequential MS2 scans at a resolution of 15,000. Data generated by LC-MS/MS were searched using the Andromeda search engine integrated into the MaxQuant (Cox et al. 2008) bioinformatic pipelines against the Uniprot *Mus musculus* reference proteome (UP000000589 9606) and then filtered using a “decoy” database-estimated false discovery rate (FDR) < 1%. Label-free quantification (LFQ) was carried out by integrating the total extracted ion chromatogram (XIC) of peptide precursor ions from the MS1 scan. These LFQ intensity values were used for protein quantification across samples. Statistical analysis of differentially expressed proteins was done using Bioconductor package ArtMS with integrated MSStats. Samples were normalized by median intensity. Proteomics data has been deposited at PRIDE with accession number PXD030021.

Acute brain slice preparation and electrophysiology—Coronal striatal slices were prepared from 10–11 week old R6/2 and NCAR mice injected with *hSyn1*-ZFPDelta-HA-tdTomato-WPRE or *hSyn1*-ZFP30645-HA-tdTomato-WPRE or *GfaABC$_1$D*-ZFPDelta-HA-tdTomato-WPRE or *GfaABC$_1$D*-ZFP30645-HA-tdTomato-WPRE AAVs in the striatum. Briefly, animals were deeply anesthetized with isoflurane and decapitated. The brains were placed and sliced in ice-cold modified artificial CSF (aCSF) containing the following (in mM): 194 sucrose, 30 NaCl, 4.5 KCl, 1 $MgCl_2$, 26 $NaHCO_3$, 1.2 NaH_2PO_4, and 10 D-glucose, saturated with 95% O_2 and 5% CO_2. A vibratome (DSK-Zero1) was used to cut 300 μm brain sections. The slices were allowed to equilibrate for 30 min at 32–34°C in normal aCSF containing (in mM); 124 NaCl, 4.5 KCl, 2 $CaCl_2$, 1 $MgCl_2$, 26 $NaHCO_3$, 1.2 NaH_2PO_4, and 10 D-glucose continuously bubbled with 95% O_2 and 5% CO_2. Slices were then allowed to return to room temperature and stored at 21–23°C in the same buffer. Slices were placed in the recording chamber and continuously perfused with 95% O_2 and 5% CO_2 bubbled normal aCSF. pCLAMP10 software and a Multi-Clamp 700B amplifier was used for electrophysiology (Molecular Devices). Whole-cell patch-clamp recordings were made from medium spiny neurons (MSNs) in the striatum using pipettes with a typical resistance of 5–6 MΩ. MSNs were identified based on tdTomato fluorescence. The intracellular solution comprised the following (in mM): 135 potassium gluconate, 5 KCl, 0.5 $CaCl_2$, 5 HEPES, 5 EGTA, 2 Mg-ATP and 0.3 Na-GTP, pH 7.3 adjusted with KOH. All recordings were performed at room temperature, using pCLAMP10 (Axon Instruments, Molecular Devices) and a MultiClamp 700B amplifier (Axon Instruments, Molecular Devices). Cells with access resistance exceeding 20 MΩ were excluded from analysis. Analysis was performed using ClampFit 10.4 software.

Lifespan assessment—A specific experiment was approved by the local Animal Research Committee to assess lifespan. R6/2 and NCAR mice were injected with AAV-PHP.eB-N-Delta [*hSyn1*-ZFPDelta-HA-tdTomato-WPRE (2.0×10^{13} GC/ml)] or AAV-PHP.eB-N-ZFP [*hSyn1*-ZFP30645-HA-tdTomato-WPRE (2.1×10^{13} GC/ml)] at 4 weeks old. The nesting assay was performed once a week. All the mice were provided with wet food on the bedding starting 8 weeks old. Mice were followed until they died of natural causes and their lifespan in days was recorded.

QUANTIFICATION AND STATISTICAL ANALYSIS

Statistical tests: Statistical tests were run in OriginPro 2016. Summary data are presented as mean ± s.e.m. For each set of data to be compared, we determined within OriginPro whether the data were normally distributed or not. If they were normally distributed, we used parametric tests. If the data were not normally distributed, we used non-parametric tests. Paired or unpaired Student's t test, Wilcoxon signed-rank test or Mann-Whitney tests were used for statistical analyses with two samples (as appropriate). Two-way ANOVA tests followed by Bonferroni's post-hoc test or Kruskal-Wallis test was used for statistical analyses with more than three samples. Significance was declared at $P < 0.05$. In the figures, P values were stated by asterisk(s): *, $P < 0.05$; **, $P < 0.01$; ***, $P < 0.001$; ****, $P < 0.0001$. The number of replicates (n values), exact P values, sample numbers and details of statistical analyses in each case are stated in Supplementary information Excel file S8 for every experiment. Raw data used to generate the figures are provided in Supplementary information Excel file S7.

Software used: Differential gene expression and enrichment analysis used R package limmaVoom to process RNA counts (https://rdrr.io/bioc/limma/man/voom.html) and batch correction was done with R package ComBat (https://rdrr.io/bioc/sva/man/ComBat.html). STRING analysis was performed using Cytoscape 3.8.2 (https://cytoscape.org/) and STRING database (https://string-db.org/). Proteomic database searches were done using version 2.0.3.0 of MaxQuant software (https://maxquant.org/). Statistical analysis of Maxquant output was carried out through artMS Bioconductor package (https://bioconductor.org/packages/artMS/), which performs the relative quantification of protein abundance using the MSstats Bioconductor package (https://msstats.org).

ADDITIONAL RESOURCES

Raw and normalized RNA-seq data from all experimental groups in this study have been deposited in the Gene Expression Omnibus repository with accession number GSE189647. RNA-seq FPKM values are also provided in Supplementary information Excel files S1–4. Proteomic data have been deposited at PRIDE with accession number PXD030021. Proteomic data are also provided in Supplementary information Excel files S5–6. All statistical tests are reported in full in Supplementary Excel file S7 for every experiment.

Supplementary Material

Refer to Web version on PubMed Central for supplementary material.

Acknowledgments

JSS was supported by the NSF Graduate Research Fellowship Program (NSF-GRFP # DGE-2034835), by the UCLA Eugene V. Cota-Robles Fellowship and partly by Khakh lab funds. This work was supported by CHDI and partly the National Institutes of Health (R35NS111583 to BSK), the Ressler Family Foundation, and the Allen Distinguished Investigator Award, a Paul G. Allen Frontiers Group advised grant of the Paul G. Allen Family Foundation. Thanks to Fuying Gao for assistance with RNA-seq data processing, and the UCLA Neuroscience Genomics Core for assistance with sequencing data generation. Thanks to HDinHD for sharing human data. Many thanks to Drs. R Cachope, V Beaumont and I Munoz-Sanjuan (CHDI) for discussions. Thanks to Gillian P Bates for sharing the Ly6a genotyping protocol via CHDI. Thanks to Blanca Diaz-Castro and Xinzhu Yu for discussions.

References

1. Bates GP, Dorsey R, Gusella JF, Hayden MR, Kay C, Leavitt BR, Nance M, Ross CA, Scahill RI, Wetzel R, et al. (2015). Huntington disease. Nature Reviews Disease Primers 1, 15005. 10.1038/nrdp.2015.5.
2. The-Huntington's-Disease-Collaborative-Research-Group (1993). A novel gene containing a trinucleotide repeat that is expanded and unstable on Huntington's disease chromosomes. The Huntington's Disease Collaborative Research Group. Cell 72, 971–983. 10.1016/0092-8674(93)90585-e. [PubMed: 8458085]
3. Munoz-Sanjuan I, and Bates GP (2011). The importance of integrating basic and clinical research toward the development of new therapies for Huntington disease. The Journal of clinical investigation 121, 476–483. 10.1172/jci45364. [PubMed: 21285520]
4. Tabrizi SJ, Langbehn DR, Leavitt BR, Roos RA, Durr A, Craufurd D, Kennard C, Hicks SL, Fox NC, Scahill RI, et al. (2009). Biological and clinical manifestations of Huntington's disease in the longitudinal TRACK-HD study: cross-sectional analysis of baseline data. The Lancet. Neurology 8, 791–801. 10.1016/s1474-4422(09)70170-x. [PubMed: 19646924]
5. Landwehrmeyer GB, McNeil SM, Dure L.S.t., Ge P, Aizawa H, Huang Q, Ambrose CM, Duyao MP, Bird ED, Bonilla E, and et al. (1995). Huntington's disease gene: regional and cellular expression in brain of normal and affected individuals. Annals of neurology 37, 218–230. 10.1002/ana.410370213. [PubMed: 7847863]
6. Lee H, Fenster RJ, Pineda SS, Gibbs WS, Mohammadi S, Davila-Velderrain J, Garcia FJ, Therrien M, Novis HS, Gao F, et al. (2020). Cell Type-Specific Transcriptomics Reveals that Mutant Huntingtin Leads to Mitochondrial RNA Release and Neuronal Innate Immune Activation. Neuron 107, 891–908.e898. 10.1016/j.neuron.2020.06.021. [PubMed: 32681824]
7. Langfelder P, Cantle JP, Chatzopoulou D, Wang N, Gao F, Al-Ramahi I, Lu XH, Ramos EM, El-Zein K, Zhao Y, et al. (2016). Integrated genomics and proteomics define huntingtin CAG length-dependent networks in mice. Nature neuroscience 19, 623–633. 10.1038/nn.4256. [PubMed: 26900923]
8. Jansen AH, van Hal M, Op den Kelder IC, Meier RT, de Ruiter AA, Schut MH, Smith DL, Grit C, Brouwer N, Kamphuis W, et al. (2017). Frequency of nuclear mutant huntingtin inclusion formation in neurons and glia is cell-type-specific. Glia 65, 50–61. 10.1002/glia.23050. [PubMed: 27615381]
9. Shin JY, Fang ZH, Yu ZX, Wang CE, Li SH, and Li XJ (2005). Expression of mutant huntingtin in glial cells contributes to neuronal excitotoxicity. The Journal of cell biology 171, 1001–1012. 10.1083/jcb.200508072. [PubMed: 16365166]
10. Tong X, Ao Y, Faas GC, Nwaobi SE, Xu J, Haustein MD, Anderson MA, Mody I, Olsen ML, Sofroniew MV, and Khakh BS (2014). Astrocyte Kir4.1 ion channel deficits contribute to neuronal dysfunction in Huntington's disease model mice. Nature neuroscience 17, 694–703. [PubMed: 24686787]
11. Khakh BS, Beaumont V, Cachope R, Munoz-Sanjuan I, Goldman SA, and Grantyn R (2017). Unravelling and Exploiting Astrocyte Dysfunction in Huntington's Disease. Trends Neurosci 40, 422–437. [PubMed: 28578789]
12. Raymond LA, André VM, Cepeda C, Gladding CM, Milnerwood AJ, and Levine MS (2011). Pathophysiology of Huntington's disease: time-dependent alterations in synaptic and receptor function. Neuroscience 198, 252–273. 10.1016/j.neuroscience.2011.08.052. [PubMed: 21907762]

13. Plotkin JL, and Surmeier DJ (2015). Corticostriatal synaptic adaptations in Huntington's disease. Current opinion in neurobiology 33, 53–62. 10.1016/j.conb.2015.01.020. [PubMed: 25700146]

14. Zeitler B, Froelich S, Marlen K, Shivak DA, Yu Q, Li D, Pearl JR, Miller JC, Zhang L, Paschon DE, et al. (2019). Allele-selective transcriptional repression of mutant HTT for the treatment of Huntington's disease. Nature medicine 25, 1131–1142. 10.1038/s41591-019-0478-3.

15. Diaz-Castro B, Gangwani M, Yu X, Coppola G, and Khakh BS (2019). Astrocyte molecular signatures in Huntington's disease. Science translational medicine 11(514). pii: eaaw8546. doi: 10.1126/scitranslmed.aaw8546. [PubMed: 31619545]

16. Mangiarini L, Sathasivam K, Seller M, Cozens B, Harper A, Hetherington C, Lawton M, Trottier Y, Lehrach H, Davies SW, and Bates GP (1996). Exon 1 of the HD gene with an expanded CAG repeat is sufficient to cause a progressive neurological phenotype in transgenic mice. Cell 87, 493–506. [PubMed: 8898202]

17. Kaye J, Reisine T, and Finkbeiner S (2021). Huntington's disease mouse models: unraveling the pathology caused by CAG repeat expansion. Faculty reviews 10, 77. 10.12703/r/10-77. [PubMed: 34746930]

18. Ghavami A, Olsen M, Kwan M, Beltran J, Shea J, Ramboz S, Duan W, Lavery D, Howland D, and Park LC (2020). Transcriptional Assessment of Striatal mRNAs as Valid Biomarkers of Disease Progression in Three Mouse Models of Huntington's Disease. Journal of Huntington's disease 9, 13–31. 10.3233/jhd-190389.

19. Bertoglio D, Verhaeghe J, Wyffels L, Miranda A, Stroobants S, Mrzljak L, Dominguez C, Skinbjerg M, Bard J, Liu L, et al. (2022). Synaptic Vesicle Glycoprotein 2A Is Affected in the Central Nervous System of Mice with Huntington Disease and in the Brain of a Human with Huntington Disease Postmortem. Journal of nuclear medicine : official publication, Society of Nuclear Medicine 63, 942–947. 10.2967/jnumed.121.262709. [PubMed: 34531262]

20. Beaumont V, Zhong S, Lin H, Xu W, Bradaia A, Steidl E, Gleyzes M, Wadel K, Buisson B, Padovan-Neto FE, et al. (2016). Phosphodiesterase 10A Inhibition Improves Cortico-Basal Ganglia Function in Huntington's Disease Models. Neuron 92, 1220–1237. 10.1016/j.neuron.2016.10.064. [PubMed: 27916455]

21. Russell DS, Jennings DL, Barret O, Tamagnan GD, Carroll VM, Caillé F, Alagille D, Morley TJ, Papin C, Seibyl JP, and Marek KL (2016). Change in PDE10 across early Huntington disease assessed by [18F]MNI-659 and PET imaging. Neurology 86, 748–754. 10.1212/wnl.0000000000002391. [PubMed: 26802091]

22. Lu AT, Narayan P, Grant MJ, Langfelder P, Wang N, Kwak S, Wilkinson H, Chen RZ, Chen J, Simon Bawden C, et al. (2020). DNA methylation study of Huntington's disease and motor progression in patients and in animal models. Nature communications 11, 4529. 10.1038/s41467-020-18255-5.

23. Shankaran M, Di Paolo E, Leoni V, Caccia C, Ferrari Bardile C, Mohammed H, Di Donato S, Kwak S, Marchionini D, Turner S, et al. (2017). Early and brain region-specific decrease of de novo cholesterol biosynthesis in Huntington's disease: A cross-validation study in Q175 knock-in mice. Neurobiology of disease 98, 66–76. 10.1016/j.nbd.2016.11.013. [PubMed: 27913290]

24. Heikkinen T, Bragge T, Bhattarai N, Parkkari T, Puoliväli J, Kontkanen O, Sweeney P, Park LC, and Munoz-Sanjuan I (2020). Rapid and robust patterns of spontaneous locomotor deficits in mouse models of Huntington's disease. PloS one 15, e0243052. 10.1371/journal.pone.0243052. [PubMed: 33370315]

25. Garland H, Wood NI, Skillings EA, Detloff PJ, Morton AJ, and Grant RA (2018). Characterisation of progressive motor deficits in whisker movements in R6/2, Q175 and Hdh knock-in mouse models of Huntington's disease. Journal of neuroscience methods 300, 103–111. 10.1016/j.jneumeth.2017.04.020. [PubMed: 28472678]

26. Alexandrov V, Brunner D, Menalled LB, Kudwa A, Watson-Johnson J, Mazzella M, Russell I, Ruiz MC, Torello J, Sabath E, et al. (2016). Large-scale phenome analysis defines a behavioral signature for Huntington's disease genotype in mice. Nature biotechnology 34, 838–844. 10.1038/nbt.3587.

27. Menalled LB, Kudwa AE, Miller S, Fitzpatrick J, Watson-Johnson J, Keating N, Ruiz M, Mushlin R, Alosio W, McConnell K, et al. (2012). Comprehensive behavioral and molecular

characterization of a new knock-in mouse model of Huntington's disease: zQ175. PloS one 7, e49838. 10.1371/journal.pone.0049838. [PubMed: 23284626]

28. Yu X, Taylor AMW, Nagai J, Golshani P, Evans CJ, Coppola G, and Khakh BS (2018). Reducing astrocyte calcium signaling in vivo alters striatal microcircuits and causes repetitive behavior. Neuron 99, 1170–1187. [PubMed: 30174118]
29. Yu X, Nagai J, Marti-Solano M, Soto JS, Coppola G, Babu MM, and Khakh BS (2020). Context-Specific Striatal Astrocyte Molecular Responses Are Phenotypically Exploitable. Neuron 108, 1146–1162.e1110. 10.1016/j.neuron.2020.09.021. [PubMed: 33086039]
30. Hodges A, Strand AD, Aragaki AK, Kuhn A, Sengstag T, Hughes G, Elliston LA, Hartog C, Goldstein DR, Thu D, et al. (2006). Regional and cellular gene expression changes in human Huntington's disease brain. Human molecular genetics 15, 965–977. 10.1093/hmg/ddl013. [PubMed: 16467349]
31. Liddelow SA, Guttenplan KA, Clarke LE, Bennett FC, Bohlen CJ, Schirmer L, Bennett ML, Münch AE, Chung WS, Peterson TC, et al. (2017). Neurotoxic reactive astrocytes are induced by activated microglia. Nature 541, 481–487. [PubMed: 28099414]
32. Kacher R, Mounier C, Caboche J, and Betuing S (2022). Altered Cholesterol Homeostasis in Huntington's Disease. Frontiers in aging neuroscience 14, 797220. 10.3389/fnagi.2022.797220. [PubMed: 35517051]
33. Benraiss A, Mariani JN, Osipovitch M, Cornwell A, Windrem MS, Villanueva CB, Chandler-Militello D, and Goldman SA (2021). Cell-intrinsic glial pathology is conserved across human and murine models of Huntington's disease. Cell reports 36, 109308. 10.1016/j.celrep.2021.109308. [PubMed: 34233199]
34. Chan KY, Jang MJ, Yoo BB, Greenbaum A, Ravi N, Wu WL, Sánchez-Guardado L, Lois C, Mazmanian SK, Deverman BE, and Gradinaru V (2017). Engineered AAVs for efficient noninvasive gene delivery to the central and peripheral nervous systems. Nature neuroscience 20, 1172–1179. 10.1038/nn.4593. [PubMed: 28671695]
35. Smith EJ, Farshim PP, Flomen R, Jones ST, McAteer SJ, Deverman BE, Gradinaru V, and Bates GP (2021). Use of high-content imaging to quantify transduction of AAV-PHP viruses in the brain following systemic delivery. Brain communications 3, fcab105. 10.1093/braincomms/fcab105. [PubMed: 34131644]
36. Woodman B, Butler R, Landles C, Lupton MK, Tse J, Hockly E, Moffitt H, Sathasivam K, and Bates GP (2007). The Hdh(Q150/Q150) knock-in mouse model of HD and the R6/2 exon 1 model develop comparable and widespread molecular phenotypes. Brain research bulletin 72, 83–97. 10.1016/j.brainresbull.2006.11.004. [PubMed: 17352931]
37. Obenauer JC, Chen J, Andreeva V, Aaronson JS, Lee R, Caricasole A, and Rosinski J (2022). Expression analysis of Huntington disease mouse models reveals robust striatum disease signatures. bioRxiv, 2022.2002.2004.479180. 10.1101/2022.02.04.479180.
38. Rattray I, Smith E, Gale R, Matsumoto K, Bates GP, and Modo M (2013). Correlations of behavioral deficits with brain pathology assessed through longitudinal MRI and histopathology in the R6/2 mouse model of HD. PloS one 8, e60012. 10.1371/journal.pone.0060012. [PubMed: 23593159]
39. Hoffner G, Island ML, and Djian P (2005). Purification of neuronal inclusions of patients with Huntington's disease reveals a broad range of N-terminal fragments of expanded huntingtin and insoluble polymers. Journal of neurochemistry 95, 125–136. 10.1111/j.1471-4159.2005.03348.x. [PubMed: 16181417]
40. Sathasivam K, Neueder A, Gipson TA, Landles C, Benjamin AC, Bondulich MK, Smith DL, Faull RL, Roos RA, Howland D, et al. (2013). Aberrant splicing of HTT generates the pathogenic exon 1 protein in Huntington disease. Proc Natl Acad Sci U S A 110, 2366–2370. 10.1073/pnas.1221891110. [PubMed: 23341618]
41. Neueder A, Dumas AA, Benjamin AC, and Bates GP (2018). Regulatory mechanisms of incomplete huntingtin mRNA splicing. Nature communications 9, 3955. 10.1038/s41467-018-06281-3.
42. Neueder A, Landles C, Ghosh R, Howland D, Myers RH, Faull RLM, Tabrizi SJ, and Bates GP (2017). The pathogenic exon 1 HTT protein is produced by incomplete splicing in Huntington's disease patients. Scientific reports 7, 1307. 10.1038/s41598-017-01510-z. [PubMed: 28465506]

43. Franich NR, Hickey MA, Zhu C, Osborne GF, Ali N, Chu T, Bove NH, Lemesre V, Lerner RP, Zeitlin SO, et al. (2019). Phenotype onset in Huntington's disease knock-in mice is correlated with the incomplete splicing of the mutant huntingtin gene. Journal of neuroscience research 97, 1590–1605. 10.1002/jnr.24493. [PubMed: 31282030]
44. Papadopoulou AS, Gomez-Paredes C, Mason MA, Taxy BA, Howland D, and Bates GP (2019). Extensive Expression Analysis of Htt Transcripts in Brain Regions from the zQ175 HD Mouse Model Using a QuantiGene Multiplex Assay. Scientific reports 9, 16137. 10.1038/s41598-019-52411-2. [PubMed: 31695145]
45. Myers RH, Vonsattel JP, Paskevich PA, Kiely DK, Stevens TJ, Cupples LA, Richardson EP Jr., and Bird ED (1991). Decreased neuronal and increased oligodendroglial densities in Huntington's disease caudate nucleus. Journal of neuropathology and experimental neurology 50, 729–742. 10.1097/00005072-199111000-00005. [PubMed: 1836225]
46. Chai H, Diaz-Castro B, Shigetomi E, Monte E, Octeau JC, Yu X, Cohn W, Rajendran PS, Vondriska TM, Whittelegge JP, et al. (2017). Neural circuit-specialized astrocytes: transcriptomic, proteomic, morphological and functional evidence. Neuron 95, 531–549. [PubMed: 28712653]
47. Srinivasan R, Lu T-Y, Chai H, Xu J, Huang BS, Golshani P, Coppola G, and Khakh BS (2016). New Transgenic Mouse Lines for Selectively Targeting Astrocytes and Studying Calcium Signals in Astrocyte Processes In Situ and In Vivo. Neuron 92, 1181–1195. [PubMed: 27939582]
48. Birolini G, Valenza M, Ottonelli I, Passoni A, Favagrossa M, Duskey JT, Bombaci M, Vandelli MA, Colombo L, Bagnati R, et al. (2021). Insights into kinetics, release, and behavioral effects of brain-targeted hybrid nanoparticles for cholesterol delivery in Huntington's disease. Journal of controlled release : official journal of the Controlled Release Society 330, 587–598. 10.1016/j.jconrel.2020.12.051. [PubMed: 33412229]
49. Birolini G, Verlengia G, Talpo F, Maniezzi C, Zentilin L, Giacca M, Conforti P, Cordiglieri C, Caccia C, Leoni V, et al. (2021). SREBP2 gene therapy targeting striatal astrocytes ameliorates Huntington's disease phenotypes. Brain : a journal of neurology. 10.1093/brain/awab186.
50. Leoni V, Mariotti C, Nanetti L, Salvatore E, Squitieri F, Bentivoglio AR, Bandettini di Poggio M, Piacentini S, Monza D, Valenza M, et al. (2011). Whole body cholesterol metabolism is impaired in Huntington's disease. Neuroscience letters 494, 245–249. 10.1016/j.neulet.2011.03.025. [PubMed: 21406216]
51. Leoni V, Mariotti C, Tabrizi SJ, Valenza M, Wild EJ, Henley SM, Hobbs NZ, Mandelli ML, Grisoli M, Björkhem I, et al. (2008). Plasma 24S-hydroxycholesterol and caudate MRI in pre-manifest and early Huntington's disease. Brain : a journal of neurology 131, 2851–2859. 10.1093/brain/awn212. [PubMed: 18772220]
52. Valenza M, Marullo M, Di Paolo E, Cesana E, Zuccato C, Biella G, and Cattaneo E (2015). Disruption of astrocyte-neuron cholesterol cross talk affects neuronal function in Huntington's disease. Cell death and differentiation 22, 690–702. 10.1038/cdd.2014.162. [PubMed: 25301063]
53. Valenza M, Rigamonti D, Goffredo D, Zuccato C, Fenu S, Jamot L, Strand A, Tarditi A, Woodman B, Racchi M, et al. (2005). Dysfunction of the cholesterol biosynthetic pathway in Huntington's disease. The Journal of neuroscience : the official journal of the Society for Neuroscience 25, 9932–9939. 10.1523/jneurosci.3355-05.2005. [PubMed: 16251441]
54. Vallès A, Evers MM, Stam A, Sogorb-Gonzalez M, Brouwers C, Vendrell-Tornero C, Acar-Broekmans S, Paerels L, Klima J, Bohuslavova B, et al. (2021). Widespread and sustained target engagement in Huntington's disease minipigs upon intrastriatal microRNA-based gene therapy. Science translational medicine 13. 10.1126/scitranslmed.abb8920.
55. Evers MM, Miniarikova J, Juhas S, Vallès A, Bohuslavova B, Juhasova J, Skalnikova HK, Vodicka P, Valekova I, Brouwers C, et al. (2018). AAV5-miHTT Gene Therapy Demonstrates Broad Distribution and Strong Human Mutant Huntingtin Lowering in a Huntington's Disease Minipig Model. Molecular therapy : the journal of the American Society of Gene Therapy 26, 2163–2177. 10.1016/j.ymthe.2018.06.021. [PubMed: 30007561]
56. Keller CG, Shin Y, Monteys AM, Renaud N, Beibel M, Teider N, Peters T, Faller T, St-Cyr S, Knehr J, et al. (2022). An orally available, brain penetrant, small molecule lowers huntingtin levels by enhancing pseudoexon inclusion. Nature communications 13, 1150. 10.1038/s41467-022-28653-6.

57. Bhattacharyya A, Trotta CR, Narasimhan J, Wiedinger KJ, Li W, Effenberger KA, Woll MG, Jani MB, Risher N, Yeh S, et al. (2021). Small molecule splicing modifiers with systemic HTT-lowering activity. Nature communications 12, 7299. 10.1038/s41467-021-27157-z.

58. Benraiss A, Wang S, Herrlinger S, Li X, Chandler-Militello D, Mauceri J, Burm H, Toner M, Osipovitch M, Xu Q, et al. (2016). Human glia can both induce and rescue aspects of phenotype in Huntington Disease. Nature communications 7.

59. Zarringhalam K, Ka M, Kook YH, Terranova JI, Suh Y, King OD, and Um M (2012). An open system for automatic home-cage behavioral analysis and its application to male and female mouse models of Huntington's disease. Behavioural brain research 229, 216–225. 10.1016/j.bbr.2012.01.015. [PubMed: 22266926]

60. Dorner JL, Miller BR, Barton SJ, Brock TJ, and Rebec GV (2007). Sex differences in behavior and striatal ascorbate release in the 140 CAG knock-in mouse model of Huntington's disease. Behavioural brain research 178, 90–97. 10.1016/j.bbr.2006.12.004. [PubMed: 17239451]

61. Hughes CS, Moggridge S, Müller T, Sorensen PH, Morin GB, and Krijgsveld J (2019). Single-pot, solid-phase-enhanced sample preparation for proteomics experiments. Nature protocols 14, 68–85. 10.1038/s41596-018-0082-x. [PubMed: 30464214]

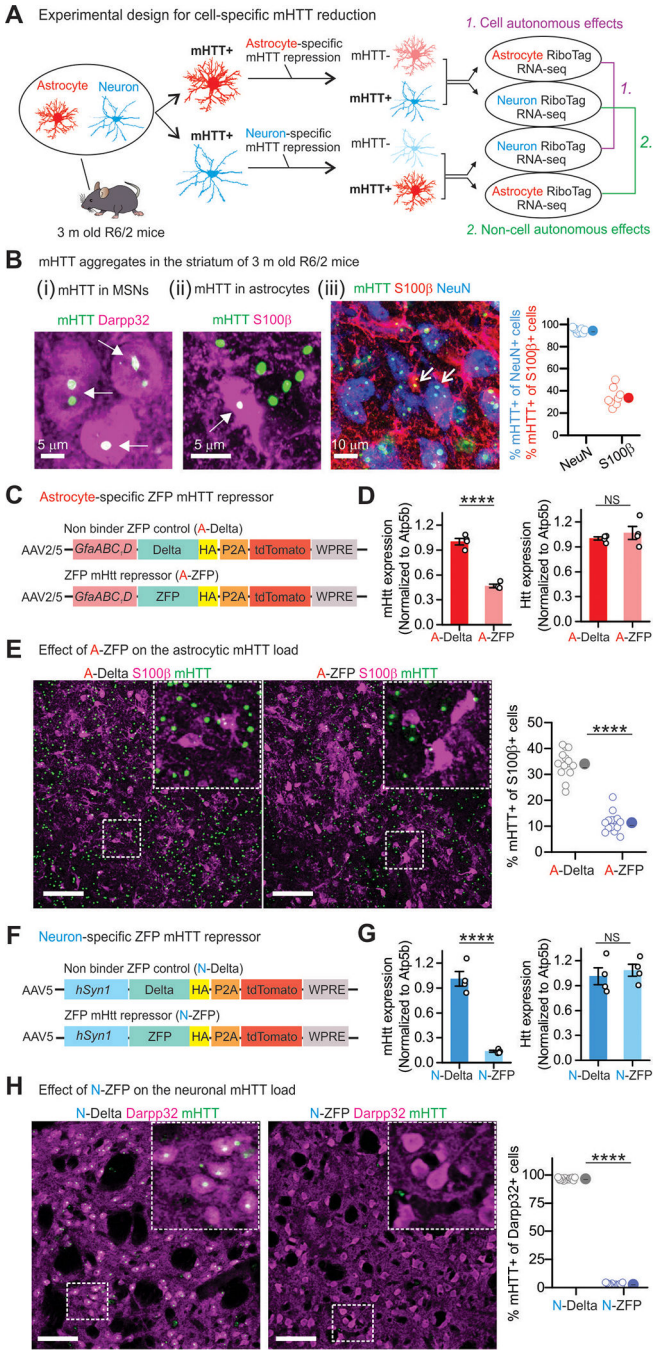

Figure 1: Striatal mHTT lowering in astrocytes and neurons in HD model mice.

(A) Experimental plan to elucidate the role of astrocytic and neuronal mHTT to HD molecular signatures in R6/2 HD model mice. (B) Representative image showing the presence of mutant huntingtin (mHTT) aggregates in neurons (NeuN) and astrocytes (S100β) within the striatum of 3 month old R6/2 mice (9 fields of view from n = 3 mice). Graph shows the percentage of NeuN+ and S100β+ cells that were also mHTT+. (C) Astrocyte specific ZFP AAVs (A-Delta and A-ZFP). A-ZFP denotes functional mHTT repressor, whereas A-Delta denotes non-binder control. (D) qPCR results showing the

reduction of mHtt, but not Htt in the astrocytic RiboTagged RNA following A-ZFP expression in the R6/2 mice (n = 4 mice). **** $P < 0.0001$; NS not significant, unpaired t test. (E) Representative images and average data for mHTT load in S100β+ striatal astrocytes of R6/2 mice (A-Delta) and the reduction of mHTT load by A-ZFP (15–16 fields of view from n = 4 mice). Scale bar is 50 μm. **** $P < 0.0001$, unpaired t test. (F) Neuron specific ZFP AAVs (N-Delta and N-ZFP). N-ZFP denotes functional mHTT repressor, whereas N-Delta denotes non-binder control. (G) qPCR results showing the reduction of mHtt but not Htt in the neuronal RiboTagged RNA following N-ZFP expression in the R6/2 mice (n = 4 mice). **** $P < 0.0001$; NS not significant, unpaired t test (H) Representative images and average data for mHTT load in Darpp32+ MSNs of the R6/2 mice (N-Delta) and the reduction of mHTT by N-ZFP (14–16 fields of view from n = 4 mice). Scale bars, 10 μm in (B), and 50 μm in (F, H). Scale bar is 50 μm. **** $P < 0.0001$, unpaired t test. Open circles are raw data and closed circles indicate mean ± SEM. **** $P < 0.0001$.

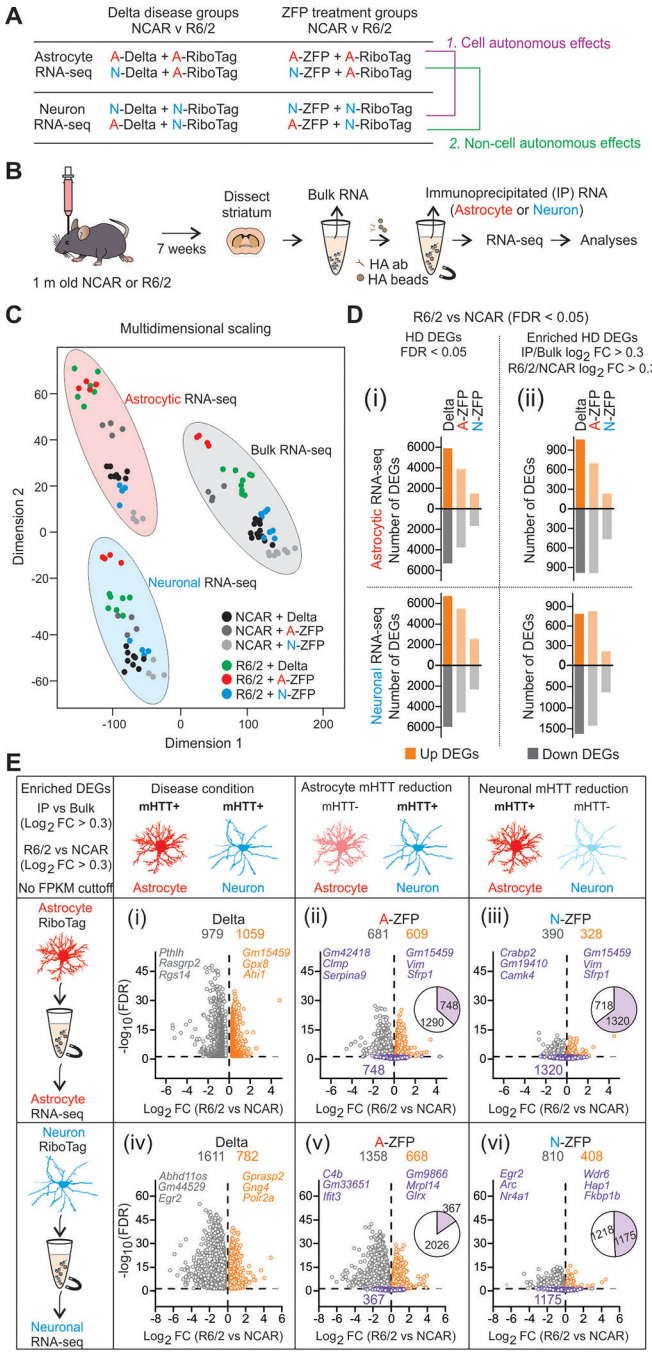

Figure 2: RNA-seq for astrocytes and neurons in HD model mice following striatal mHTT lowering.

(A-B) Experimental design to combine cell-type specific mHTT lowering with cell-type specific RNA-seq. (C) Multidimensional scaling plot depicts principal component analysis for astrocytic-specific, neuron-specific, and bulk-tissue RNA-seq in disease (Delta) and treatment (ZFP) groups (n = 3–5). (D) Bar graphs depicting the number of upregulated and downregulated differentially expressed genes (DEGs) for R6/2 mice (vs NCAR controls; FDR > 0.05) in astrocytic and neuronal RNA-seq (i). Orange denotes upregulated DEGs and gray denotes downregulated DEGs. Enrichment criterion of log2 fold change (logFC) >

0.3 in IP (vs bulk RNA-seq) and R6/2 (vs NCAR controls) was applied to provide cell-type enrichment and remove potential contamination by highly expressed genes in other cell types (ii). (E) Volcano plots depicting upregulated DEGs in orange, downregulated DEGs in grey, and those genes not differentially expressed following ZFP expressed in purple. Delta represents the disease condition in astrocyte (i) and neuron (iv) RNA-seq. A-ZFP shows the effect of astrocytic mHTT lowering on the HD DEGs in astrocytes (ii) and neurons (v) RNA-seq. N-ZFP shows the effect of neuronal mHTT lowering on the HD DEGs in astrocytes (iii) and neurons (vi) RNA-seq.

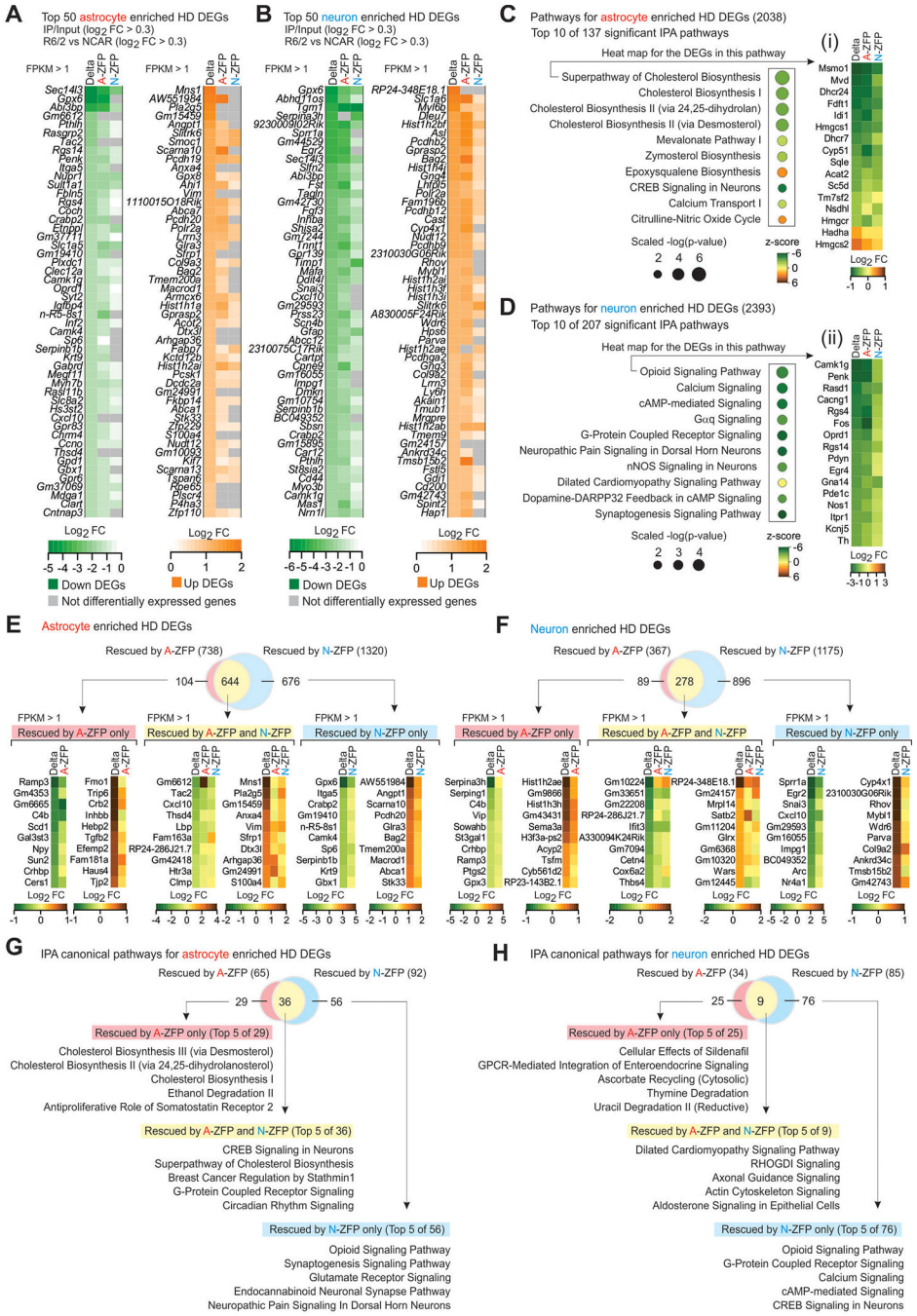

Figure 3: Cell autonomous and non-cell autonomous effects of striatal mHTT lowering.

(A) Heat map for top 50 downregulated and upregulated astrocyte enriched HD DEGs (astrocyte IP vs bulk $\log_2$FC > 0.3; R6/2 vs NCAR controls $\log_2$FC > 0.3). Green color denotes downregulated DEGs, and orange color denotes upregulated DEGs. Delta shows the $\log_2$FC for the disease condition in striatal astrocytes of R6/2 mice (vs NCAR controls), while A-ZFP and N-ZFP shows the effect of astrocytic and neuronal mHTT lowering, respectively. (B) Heat map for top 50 downregulated and upregulated neuron enriched HD DEGs (neuron IP vs bulk $\log_2$FC > 0.3; R6/2 vs NCAR controls $\log_2$FC > 0.3). Delta shows

the log_2FC for the disease condition in striatal neurons of R6/2 mice (vs NCAR controls), while A-ZFP and N-ZFP shows the effect of astrocytic and neuronal mHTT lowering, respectively. (C) Top 10 canonical pathways represented by the striatal astrocyte enriched DEGs (2038) in R6/2 mice (vs NCAR controls FDR < 0.05, log_2FC > 0.3). Scaled -log10 (p-value) was calculated for the IPA pathways by multiplying -log10 (p-value) with ratio (fraction of the genes for a particular pathway). Size of the circle represents scaled -log (p-value) and the color indicates z-score. A negative z-score denotes the inhibition of the pathway, while a positive z-score denotes the activation of the pathway. The right panel shows a heat map for the astrocytic DEGs involved in the superpathway of cholesterol biosynthesis. Color of the heat map denotes log_2FC for the striatal astrocytes in R6/2 mice (vs NCAR controls). Delta denotes the disease condition (Delta), while A-ZFP and N-ZFP shows the effect of astrocytic and neuronal mHTT lowering on the striatal astrocytes, respectively. (D) Top 10 canonical pathways represented by the enriched striatal neuron DEGs (2393) in R6/2 mice (vs NCAR controls FDR < 0.05, log_2FC > 0.3). Size of the circle represents scaled -log (p-value) and the color indicates z-score. The right panels shows a heat map for DEGs involved in the opioid signaling pathway. Color of the heat map denotes log_2FC for the striatal neurons in R6/2 mice (vs NCAR controls). Delta denotes the disease condition (Delta), while A-ZFP and N-ZFP shows the effect of astrocytic and neuronal mHTT lowering on the striatal neurons, respectively. (E) Venn diagram for the number of astrocyte enriched HD DEGs rescued by A-ZFP and N-ZFP. Overlap shows the DEGs rescued by both A-ZFP and N-ZFP. Heat maps are shown for the top 10 downregulated and upregulated astrocyte enriched HD DEGs (FPKM >1) rescued by A-ZFP only, N-ZFP only, or by both A-ZFP and N-ZFP. (F) Venn diagram for the number of neuron enriched HD DEGs rescued by A-ZFP and N-ZFP. Overlap shows the DEGs rescued by both A-ZFP and N-ZFP. Heat map for top 10 downregulated and upregulated neuron enriched HD DEGs (FPKM >1) rescued by A-ZFP only, N-ZFP only or by both A-ZFP and N-ZFP. (G) Venn diagram shows the number of IPA pathways significantly affected based on astrocyte enriched HD DEGs rescued by A-ZFP and N-ZFP. Overlap shows the pathways rescued by both A-ZFP and N-ZFP. Pathway names are shown for the top 5 pathways rescued by A-ZFP only, N-ZFP only or by both A-ZFP and N-ZFP in astrocytes. (H) Venn diagram shows the number of IPA pathways significantly affected for neuron enriched HD DEGs rescued by A-ZFP and N-ZFP. Overlap shows the number of pathways rescued by both A-ZFP and N-ZFP. Pathway names are shown for the top 5 pathways rescued by A-ZFP only, N-ZFP only or by both A-ZFP and N-ZFP in neurons.

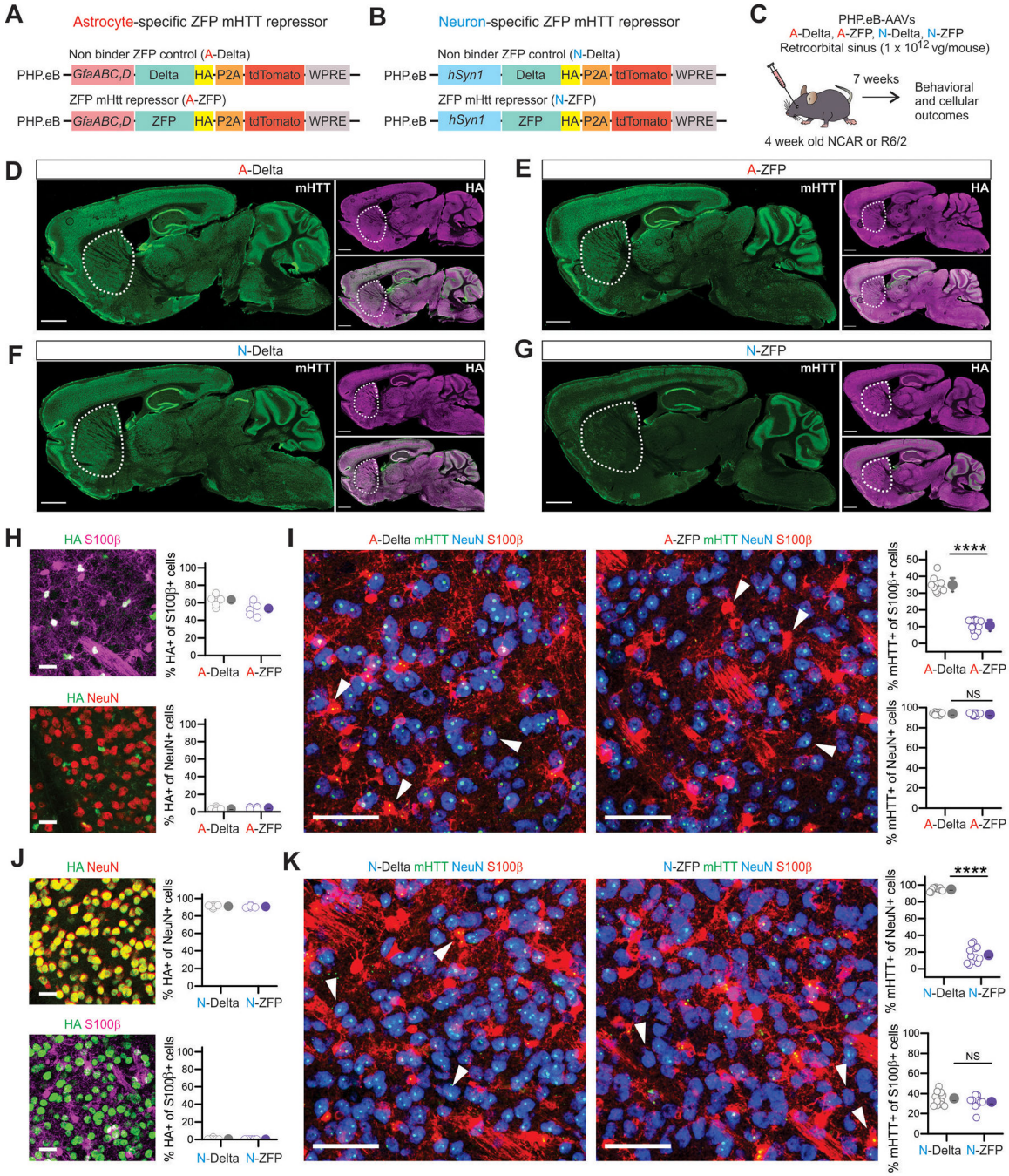

Figure 4: Brain wide mHTT lowering with ZFPs in astrocytes and neurons using PHP.eB AAVs.

(A) Schematic of astrocyte specific ZFP PHP.eB AAVs (A-Delta and A-ZFP). A-ZFP denotes functional mHTT repressor in astrocytes, whereas A-Delta denotes non-binder control. (B) Schematic of neuron specific ZFP PHP.eB AAVs (N-Delta and N-ZFP). N-ZFP denotes functional mHTT repressor in neurons, whereas N-Delta denotes control. (C) Cartoon depicting the experimental design. Briefly, astrocyte specific and neuron specific ZFP PHP.eB AAVs at 1 $\times 10^{12}$ genome copies per mouse were injected in the retro orbital sinus of R6/2 mice at 4 weeks of age and cellular outcomes assessed at 11 weeks of age. (D)

Representative images of a sagittal brain section from R6/2 mice that had been administered with PHP.eB A-Delta AAV and immunostained for mHTT and HA (representative of n = 3 mice). The images show the presence of mHTT puncta throughout the brain of R6/2 mice and co-staining for HA shows the penetrance of ZFP PHP.eB AAVs in the brain. (E) As in D, but for A-ZFP (representative of n = 3 mice). Note there are less mHTT puncta. (F) As in D, but for N-Delta (representative of n = 3 mice). (G) As in E, but for N-ZFP (n = 3 mice). Note the lower amount of mHTT puncta in comparison to panel F. (H) Representative images and quantification of astrocyte specific PHP.eB-driven ZFP colocalization with S100β+ astrocytes and NeuN+ neurons of the striatum (n = 3 mice). (I) Representative images and quantification of mHTT load in S100β+ astrocytes and NeuN+ neurons of the striatum with A-Delta and A-ZFP (n = 3 mice). **** $P < 0.0001$; NS not significant, Mann-Whitney test. (J) Representative images and quantification of neuron specific PHP.eB-driven ZFP colocalization with NeuN+ neurons and S100β+ astrocytes of the striatum (n = 3 mice). (K) Representative images and quantification of mHTT load in NeuN+ neurons and S100β+ astrocytes of the striatum with N-Delta and N-ZFP (n = 3 mice). **** $P < 0.0001$; NS not significant, unpaired t test or Mann-Whitney test. Scale bars, 1 mm in (D-G), 20 μm in (H, J) and 50 μm in (I, K). Open circles are raw data and closed circles indicate mean ± SEM. **** $P < 0.0001$, NS not significant.

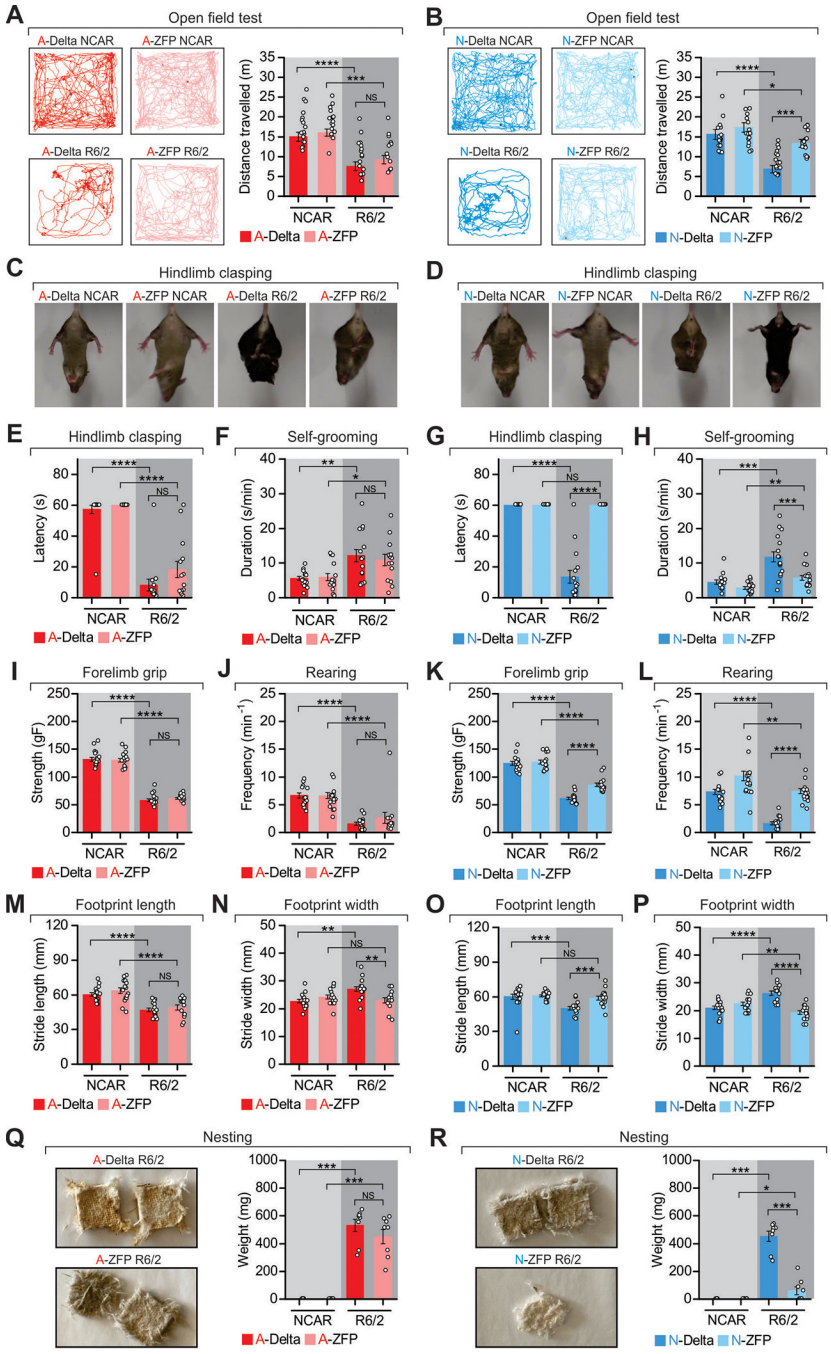

Figure 5: Brain wide mHTT lowering effects on behavioral deficits in R6/2 HD mice.

(A) Representative traces for open field tests over 10 min in NCAR and R6/2 mice injected with astrocytic (A) ZFP PHP.eB AAVs (A-Delta and A-ZFP) and neuronal (B) ZFP PHP.eB AAVs (N-Delta and N-ZFP). Bar graphs show the distance travelled by NCAR and R6/2 mice. (C,D) Representative images showing hind limb clasping behavior when the R6/2 and NCAR mice are suspended by the tail for 1 min for astrocytic (C) and neuronal (D) ZFP PHP.eB AAVs, respectively. (E,G) Time taken by the R6/2 and NCAR mice to clasp their hind limbs upon tail suspension in astrocytic (E) and neuronal (G) ZFP PHP.eB AAV

injected groups, respectively. Mice that did not clasp were given the score of 60 s. (F,H) Time spent grooming by R6/2 and NCAR mice in a cylindrical enclosure for astrocytic (f) and neuronal (h) ZFP PHP.eB AAV injected groups, respectively. (I,K) Forelimb grip strength for R6/2 and NCAR mice measured using grip-strength meter over 5 separate trials for astrocytic (I) and neuronal (K) ZFP PHP.eB AAV injected groups, respectively. (J,L) Number of rearing bouts of R6/2 and NCAR mice assessed in a cylindrical enclosure for astrocytic (J) and neuronal (L) ZFP PHP.eB AAV injected groups, respectively. (M,N) Bar graphs show stride length and stride width for R6/2 and NCAR mice injected with astrocytic PHP.eB (A-Delta and A-ZFP) AAVs. (O,P) Bar graphs show stride length and stride width for R6/2 and NCAR mice injected with neuronal PHP.eB (N-Delta and N-ZFP) AAVs. (Q,R) Representative images of the nesting material that was not used for nest building at the end of a 4d period for R6/2 mice. There was no remaining nesting material for NCAR mice, which were thus given a score of zero. The weight of the nesting material left behind in R6/2 mice was measured for astrocytic (Q) and neuronal (R) ZFP PHP.eB AAV groups, respectively. Data are shown as mean ± SEM. ****$P < 0.0001$, ***$P < 0.001$, **$P < 0.01$, *$P < 0.05$, NS not significant, two-way ANOVA followed by Bonferroni's post-hoc test (Panels A, I, L, M, N and P) or Kruskal-Wallis ANOVA (Panels B, E, F, G, H, J, K, O, Q and R). The behaviors shown in this figure are n = 14–17 mice in each group.

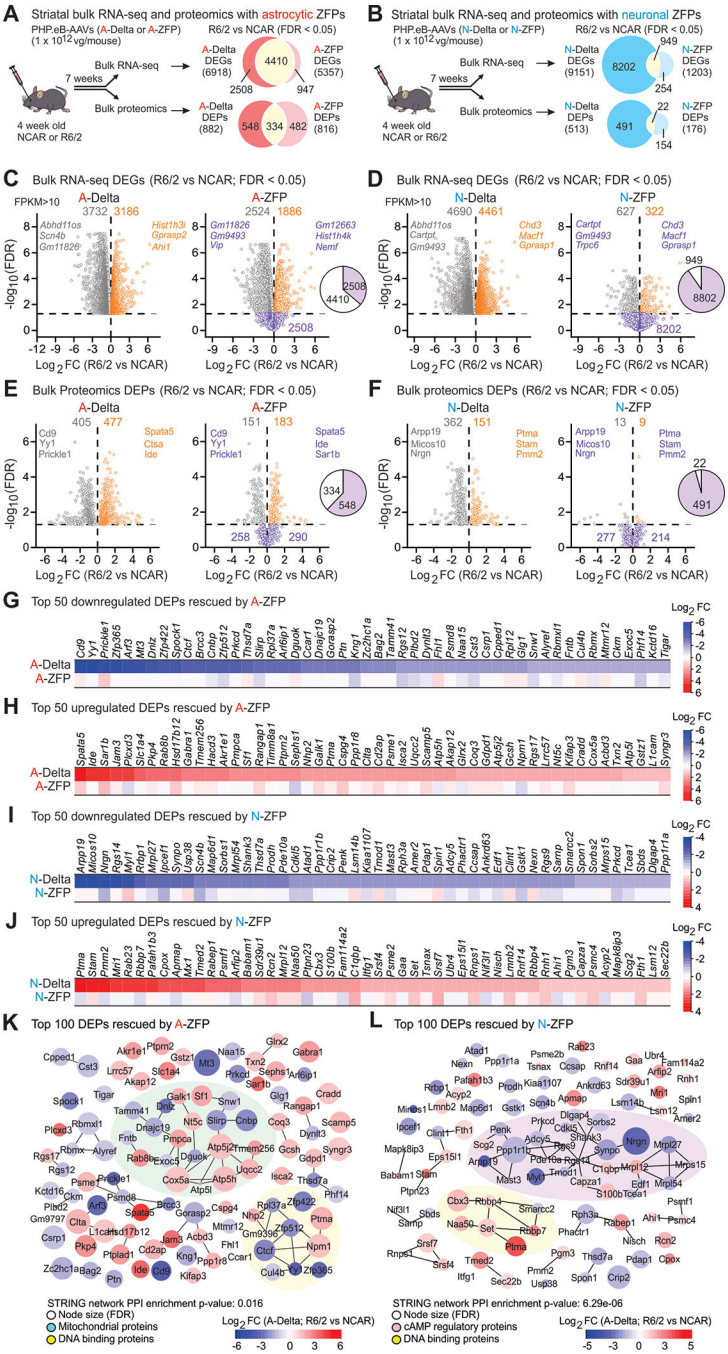

Figure 6: Brain-wide mHTT lowering effects on HD-associated striatal RNA and protein deficits.

(A, B) Cartoons depict the experimental design to test the effect of astrocytic and neuronal ZFP PHP.eB AAVs (A-Delta and A-ZFP) on the striatal bulk RNA and bulk proteome in R6/2 mice. Venn diagram depicting the number of differentially expressed genes (DEGs) and proteins (DEPs; in relation to NCAR controls; FDR < 0.05) in R6/2 mice that had received A-Delta and A-ZFP PHP.eB AAVs. (C) Volcano plot shows the log2 transformed fold-change (R6/2 vs NCAR controls) on the x-axis and negative log10 transformed adjusted p-value on the y-axis. The volcano plots depict upregulated DEGs in orange, downregulated

DEGs in gray, and the genes not differentially expressed following ZFP in purple. A-Delta shows the DEGs in the disease condition and A-ZFP shows the effect of astrocytic mHTT lowering on those disease DEGs. (D) As in C, but for the effect of neuronal mHTT lowering (N-ZFP) on the disease DEGs (N-Delta). (E) Volcano plot shows the log2 transformed fold-change (R6/2 vs NCAR controls) of LFQ intensity values on the x-axis and negative log10 transformed adjusted p-value on the y-axis. The volcano plots depict upregulated DEPs in orange, downregulated DEPs in gray, and the proteins not differentially expressed in purple. A-Delta shows the DEPs in the disease and A-ZFP shows the effect of astrocytic mHTT reduction on those disease DEPs. (F) As in C but shows the effect of neuronal mHTT lowering (N-ZFP) on the disease DEPs (N-Delta). (G) Heat map depicting top 50 downregulated DEPs in the R6/2 vs NCAR controls (FDR < 0.05) in A-Delta and rescued by A-ZFP in R6/2. (H) Heat map depicting top 50 upregulated DEPs in the R6/2 vs NCAR controls (FDR < 0.05) in A-Delta and rescued by A-ZFP in R6/2. (I) Heat map depicting top 50 downregulated DEPs in the R6/2 vs NCAR controls (FDR < 0.05) in N-Delta and rescued by N-ZFP in R6/2. (J) Heat map depicting top 50 upregulated DEPs in the R6/2 vs NCAR controls (FDR < 0.05) in N-Delta and rescued by N-ZFP in R6/2. (K) Scale-free STRING analysis network map of the top 50 downregulated and 50 upregulated proteins rescued by astrocyte ZFP (A-ZFP). Node size represents the $\log_2$LFQ abundance measure while the color of the node represents the $\log_2$fold change of A-ZFP versus A-Delta in R6/2 model mice. The two biggest interaction nodes in green and yellow represent mitochondrial and DNA binding proteins, respectively. (L) As in K, but for proteins rescued by neuron ZFP (N-ZFP). The proteomic data shown in this figure are from n = 4 mice in each group.

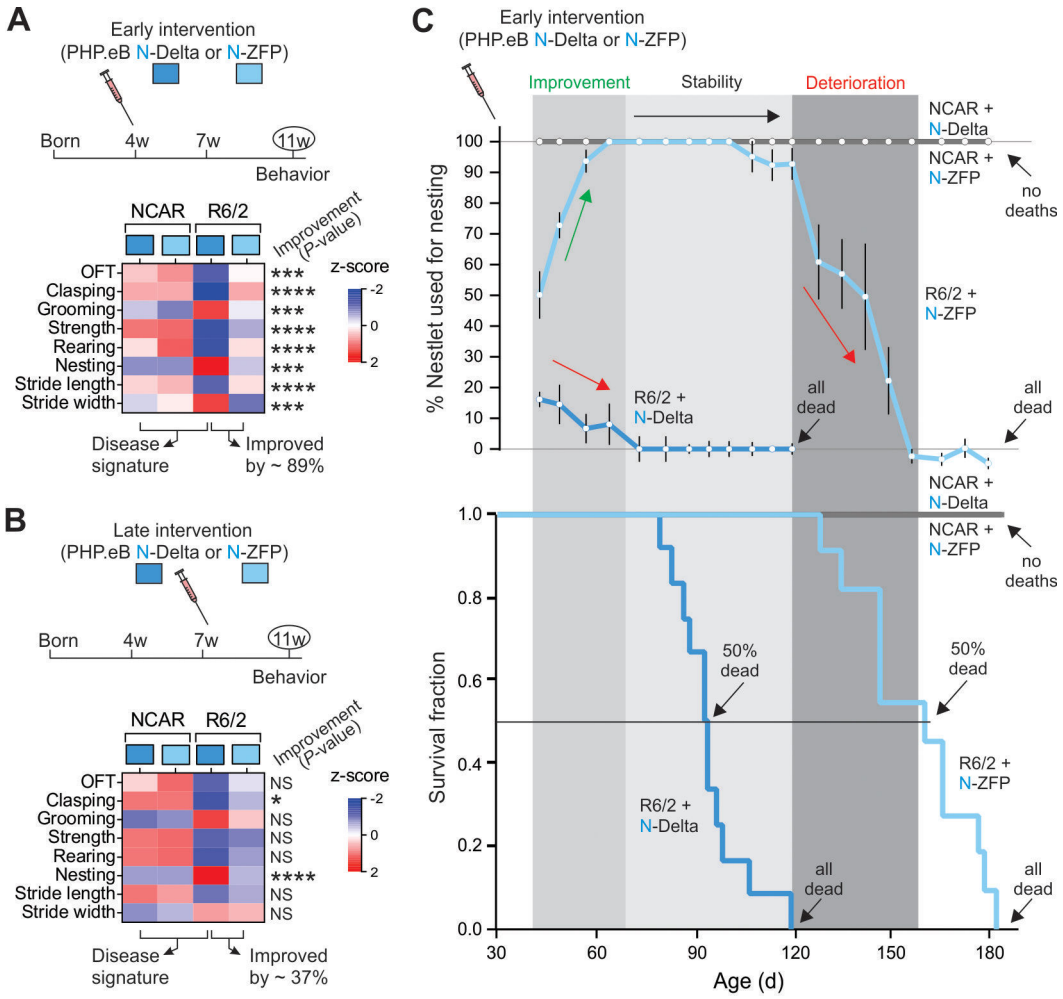

Figure 7: Brain wide N-ZFP: early *versus* late interventions and lifespan analyses.

(A) Eight different behavioral assessments were performed at 11 weeks of age on R6/2 mice and NCAR controls injected with neuron specific PHP.eB ZFP AAVs (N-Delta and N-ZFP) at 4 weeks of age (early intervention). Row z-scores were calculated for each behavior using the individual test scores in NCAR and R6/2 mice injected with N-Delta or N-ZFP PHP.eB AAV (these data are replotted from Figure 5). The asterisks indicate if the behavior shown by the row was improved by ZFPs. The lower value of ~89% improvement was based on the aggregate z-score across all behaviors. (B) As in A, but for R6/2 and NCAR mice injected with neuron specific PHP.eB ZFP AAVs (N-Delta and N-ZFP) at 7 weeks of age (late intervention). Row z-scores were calculated for each behavior using the individual test scores in NCAR and R6/2 mice injected with N-Delta or N-ZFP PHP.eB AAV (n = 5–6 mice). There were trends for improvement across the board, resulting in an aggregate z-score improvement of ~37%, although many of the individual behaviors were not improved significantly. (C) Nesting assay and lifespan assessments were performed on R6/2 mice and NCAR controls injected with neuron specific PHP.eB ZFP AAVs (N-Delta and N-ZFP) at 4 weeks of age (n = 7–12 mice).

KEY RESOURCES TABLE

REAGENT or RESOURCE	SOURCE	IDENTIFIER
Antibodies		
mouse anti-S100β	Sigma-Aldrich	Cat# S2532; RRID:AB_477499
rabbit anti-S100β	Abcam	Cat# ab41548; RRID: AB_956280
chicken anti-S100β	Synaptic Systems	Cat# 287006; RRID:AB_2713986
mouse anti-NeuN (clone A60)	Millipore	Cat# MAB377; RRID: AB_2298772
chicken anti-GFP	Abcam	Cat# ab13970; RRID: AB_300798
rabbit anti-RFP	Rockland	Cat# 600–401-379; RRID: AB_2209751
mouse anti-HA	BioLegend	Cat# 901514, RRID:AB_2565336
guinea pig anti-NeuN	Synaptic Systems	Cat# 266 004, RRID:AB_2619988
rabbit anti-NeuN	Cell Signaling Technology	Cat# 12943, RRID:AB_2630395
rabbit anti-Darpp32	Abcam	Cat# ab40801, RRID:AB_731843
mouse anti-mHTT (clone mEM48)	Millipore	Cat# MAB5374, RRID:AB_10055116
mouse anti-mHTT (clone 2B4)	Millipore	Cat# MAB5492, RRID:AB_347723
Alexa Fluor 488 goat anti-chicken	Molecular Probes	Cat# A11039; RRID: AB_2534096
Alexa Fluor 488 goat anti-rabbit	Molecular Probes	Cat# A11008; RRID: AB_143165
Alexa Fluor 546 goat anti-mouse	Molecular Probes	Cat# A11003; RRID: AB_2534071
Alexa Fluor 546 goat anti-chicken	Molecular Probes	Cat# A11040; RRID: AB_2534097
Alexa Fluor 594 goat anti-rabbit	Molecular Probes	Cat# R37117; RRID: AB_2556545
Alexa Fluor 647 goat anti-rabbit	Molecular Probes	Cat# A21245; RRID: AB_ 2535812
Bacterial and Virus Strains		
AAV2/5 *GfaABC$_1$D* Rpl22HA	Yu et al., 2018	Addgene Vectors #111811RRID:Addgene_111811
AAV5 *hSyn1* Rpl22HA	This paper	Addgene Vectors #177685RRID:Addgene_177685
AAV2/5 *GfaABC$_1$D* ZFPDeltaDBD-HA P2A tdTomato	Diaz-Castro et al, 2019	See *note 1*
AAV2/5 *GfaABC$_1$D* ZFP30645-HA P2A tdTomato	Diaz-Castro et al, 2019	See *note 1*
AAV PHP.eB *GfaABC$_1$D* ZFPDeltaDBD-HA P2A tdTomato	This paper	See *note 1*
AAV PHP.eB *GfaABC$_1$D* ZFP30645-HA P2A tdTomato	This paper	See *note 1*
AAV5 *hSyn1* ZFPDeltaDBD-HA P2A tdTtomato	This paper	See *note 1*
AAV5 *hSyn1* ZFP30645-HA P2A tdTomato	This paper	See *note 1*
AAV PHP.eB *hSyn1* ZFPDeltaDBD-HA P2A tdTomato	This paper	See *note 1*
AAV PHP.eB *hSyn1* ZFP30645-HA P2A tdTomato	This paper	See *note 1*
Chemicals, Peptides, and Recombinant Proteins		
Formalin, Buffered, 10%	Fisher Chemical	Cat# SF100–20
Pronase	Sigma-Aldrich	Cat# P6911
Fetal bovine serum	Thermo Fisher Scientific	Cat# 10437028
BSA	Sigma-Aldrich	Cat# A8806

REAGENT or RESOURCE	SOURCE	IDENTIFIER
Phosphate buffered saline	Sigma-Aldrich	Cat# P4417–100TAB
Formic acid	Sigma-Aldrich	Cat# 695076
Experimental Models: Organisms/Strains		
Mouse: B6CBA-Tg(HDexon1)62Gpb/3J	Jackson Laboratory	Stock# 006494; RRID:IMSR_JAX:006494
Mouse: B6J.129S1-Htttm1Mfc/190ChdiJ	Jackson Laboratory	Stock# 027410; RRID:IMSR_JAX:027410
Mouse: C57Bl/6NJ	Jackson Laboratory	Stock# 005304; RRID:IMSR_JAX:005304
Mouse: C57Bl/6NTac inbred mice	Taconic	Stock# B6; RRID:IMSR_TAC:b6
Oligonucleotides		
C57insF (5'-CTGGAATTAGGAATGGTTGTGTG-3')	Smith et al., 2021	N/A
C57insR (5'-TTGTTCTTTACTTTCCTTGTTTGAGAAT-3')	Smith et al., 2021	N/A
CBAinsF2 (5'-TAGGAATGGTTGTAAACCAGG-3')	Smith et al., 2021	N/A
CBAinsR2 (5'-CCTCCATTGGGAACTGCTG-3')	Smith et al., 2021	N/A
Mutant Htt forward (5'-CGCAGGCTGCAGGGTTAC-3')	Zeitler et al., 2019	N/A
Mutant Htt reverse (5'-GCTGCACCGACCGTGAGT-3')	Zeitler et al., 2019	N/A
Mutant Htt prove (5'-CAGCTCCCTGTCCCGGCGG-3')	Zeitler et al., 2019	N/A
Atp5b (Mm.PT.53a.17279462)	Integrated DNA Technologies, Inc.	N/A
Htt (Mm.PT.58.6953479)	Integrated DNA Technologies, Inc.	N/A
Software and Algorithms		
OriginPro 2016	Origin Lab Corporation	RRID:SCR_015636
pCLAMP10.4	Molecular Devices	RRID:SCR_011323
ClampFit10.4	Molecular Devices	N/A
Fluoview FV10-ASW	Olympus	N/A
Fluoview FV31S-SW	Olympus	N/A
ImageJ v1.51h	NIH	RRID:SCR_003070
ANY-maze	Stoelting Co.	RRID:SCR_014289
MaxQuant 2.0.3.0	https://maxquant.org	RRID:SCR_014485
Cytoscape 3.8.2	https://cytoscape.org	RRID:SCR_003032
CorelDraw X7	Corel Corporation	RRID:SCR_014235
STRING database	https://string-db.org	RRID:SCR_005223
MSstats Bioconductor package	https://msstats.org	RRID:SCR_014353
Bioconductor	http://www.bionconductor.org	RRID:SCR_006442
Deposited Data		
Astrocyte, neuron and bulk RNA-seq:	This paper	GEO: GSE189647GEO: GSE211891
Bulk tissue proteomics	This paper	PRIDE: PXD030021
Statistical tests used in the figures	This paper	Excel file S7

Note 1: The vectors listed incorporating Sangamo Biosciences / Takeda Inc mHTT zinc finger repressor proteins ZFP-30645 and ZFP-DBD were made by the Khakh lab. The original plasmids were obtained via CHDI Foundation under the terms of a Use Agreement by and between CHDI

Foundation and Sangamo Biosciences. Requests for these plasmids should be made directly to CHDI Foundation (info@CHDIFoundation.org) with ZFP in the subject line.